



Kent Academic Repository

Folco, Luigi, Carone, L., D'Orazio, Massimo, Cordier, Carole, Suttle, Martin D., van Ginneken, Matthias and Masotta, M. (2022) *Microscopic impactor debris at Kamil Crater (Egypt): The origin of the Fe-Ni oxide spherules.* *Geochimica et Cosmochimica Acta* . ISSN 0016-7037.

Downloaded from

<https://kar.kent.ac.uk/97042/> The University of Kent's Academic Repository KAR

The version of record is available from

<https://doi.org/10.1016/j.gca.2022.06.035>

This document version

Author's Accepted Manuscript

DOI for this version

Licence for this version

UNSPECIFIED

Additional information

Versions of research works

Versions of Record

If this version is the version of record, it is the same as the published version available on the publisher's web site. Cite as the published version.

Author Accepted Manuscripts

If this document is identified as the Author Accepted Manuscript it is the version after peer review but before type setting, copy editing or publisher branding. Cite as Surname, Initial. (Year) 'Title of article'. To be published in *Title of Journal* , Volume and issue numbers [peer-reviewed accepted version]. Available at: DOI or URL (Accessed: date).

Enquiries

If you have questions about this document contact ResearchSupport@kent.ac.uk. Please include the URL of the record in KAR. If you believe that your, or a third party's rights have been compromised through this document please see our [Take Down policy](https://www.kent.ac.uk/guides/kar-the-kent-academic-repository#policies) (available from <https://www.kent.ac.uk/guides/kar-the-kent-academic-repository#policies>).



Contents lists available at ScienceDirect

Geochimica et Cosmochimica Acta

journal homepage: www.elsevier.com/locate/gca

Microscopic impactor debris at Kamil Crater (Egypt): The origin of the Fe-Ni oxide spherules



L. Folco^{a,b,*}, L. Carone^c, M. D'Orazio^{a,b}, C. Cordier^d, M.D. Suttle^{e,a}, M. van Ginneken^f, M. Masotta^{a,b}

^a Dipartimento di Scienze della Terra, Università di Pisa, Via S. Maria 53, Pisa, Italy

^b CISUP, Centro per la Integrazione della Strumentazione dell'Università di Pisa, Lungarno Pacinotti, Pisa, Italy

^c Università di Camerino, Scuola di Scienze e Tecnologie, Sezione di Geologia, Via Gentile III da Varano 7, 62032 Camerino, Italy

^d Université Grenoble Alpes, Université Savoie Mont Blanc, CNRS, IRD, IFSTTAR, ISTERre, 38000 Grenoble, France

^e School of Physical Sciences, The Open University, Walton Hall, Milton Keynes MK7 6AA, UK

^f Centre for Astrophysics and Planetary Science, School of Physical Sciences, Ingram Building, University of Kent, Canterbury CT2 7NH, UK

ARTICLE INFO

Article history:

Received 14 March 2022

Accepted 23 June 2022

Available online 1 July 2022

Associate editor: Christopher Herd

Keywords:

Impact spherules

Impact melting

Impact cratering

Fe-Ni oxides

Kamil crater

ABSTRACT

Kamil crater (Egypt) is a natural laboratory for the study of processes and products associated with the impacts of small iron projectiles on the Earth's crust. In particular, because of the distinctive composition of the impactor (an ungrouped Ni-rich ataxite) and the target (Cretaceous sandstones and minor wackes) it offers a unique opportunity to study impactor–target physical–chemical interactions. Continuing the study of impact melt ejecta, we investigated the mineralogy and geochemistry of 25 Fe-Ni spherules – representative of a suite of 135 – recovered from the soil around the crater. Samples were collected during our 2010 geophysical expedition and investigated by combining scanning electron microscope imaging, electron probe microanalyzer and Raman spectroscopy analyses. Spherules range in size from 100 to 500 μm and show a variety of dendritic textures and mineral compositions dominated by Fe-Ni oxides of the wüstite – bunsenite and magnetite – trevorite series or Fe-Ni metal. All these features indicate quenching of high temperature (1600–1500 $^{\circ}\text{C}$) oxide or metal liquid droplets under varying oxidizing conditions. A geochemical affinity with the iron impactor recorded by the Fe, Co, Ni ratios in the constituent phases (average Ni/Co element ratio of 25.1 ± 7.6 ; average Ni/(Ni + Fe) molar ratio of 0.21 ± 0.13), combined with target contamination (i.e., the ubiquitous occurrence of Si and Al from trace to minor amounts), document their origin as impact melt spherules formed through the physical and chemical interaction between metal projectile and silicate target melts and air. We propose a petrogenetic model that envisions formation as liquid droplet residues of immiscible projectile in a mixed silicate melt and their subsequent separation as individual spherules by stripping during hypervelocity ejection. We also argue that this model applies to all impact events produced by small iron projectiles and that such individual Fe-Ni oxide and metal spherules should be common impact products, despite little documentation in the literature. Our detailed mineralogical and geochemical characterization will facilitate their distinction from other, similar spherules of different origin (cosmic spherules, ablation spherules) often encountered in the geologic record.

© 2022 Elsevier Ltd. All rights reserved.

1. Introduction

Kamil is a small (45 m in diameter) impact crater in southwestern Egypt (22°01'06"N, 26°05'16"E). It was generated by the hypervelocity impact of a small iron meteorite (an ungrouped Ni-rich ataxite), named Gebel Kamil, on a sedimentary target (sandstones belonging to the Cretaceous Gilf Kebir

Formation) <5000 years ago (Folco et al., 2010). Due to its extraordinary state of preservation, Kamil is considered a type-structure for small impact craters on Earth and thus a natural laboratory to investigate processes and products associated with the impact of small projectiles (Folco et al., 2011).

Upon hypervelocity impact, the iron meteorite underwent catastrophic fragmentation and melting. These processes produced thousands of fragments with individual pieces up to ~ 30 kg in mass (D'Orazio et al., 2011) alongside cm-sized impact melt bombs and lapilli of impact melt glasses (Fazio et al., 2014, 2016) scattered around the crater, as well as microscopic impactor debris dispersed

* Corresponding author at: Dipartimento di Scienze della Terra, Università di Pisa, Via S. Maria 53, Pisa, Italy.

E-mail address: luigi.folco@unipi.it (L. Folco).

within the ejecta blanket and surrounding soil (Urbini et al., 2012). The former consists of white (almost pure silica) to dark (Fe-Si-Al-rich) glasses, which are mixtures of target and impactor materials to varying degrees. The latter include vesicular particles of white glass and spherules and coatings of dark glasses, plus Fe-Ni spherules and mini shrapnel (Folco et al., 2015).

In this work we focus on the nature of the microscopic Fe-Ni oxide spherules which were only described preliminarily by Folco et al. (2015). From a batch of 135 spherules extracted from soil samples collected around the crater during our geophysical expedition in 2010 and imaged under the scanning electron microscope, we selected a representative set of 25 Fe-Ni particles in the 100–500 μm size range for a detailed mineralogical and geochemical investigation combining electron microscope imaging, electron probe microanalyzer and Raman spectroscopy analyses.

Data reveal a variety of textures, compositions and oxidation states that largely expands the previous inventory of Folco et al. (2015), are consistent with an impact origin, and provide the basis for discussing a general formation mechanism during hypervelocity impacts of iron projectiles. In particular, we propose a petrogenetic model which envisions a sequence of processes from disequilibrium impact melting at the target-projectile interface, oxidation, liquid mixing/immiscibility, chemical fractionation at the end of the contact and compression stage, to the aerodynamic physical separation of the immiscible components of the impact melt during ejection in the excavation stage.

Similar individual Fe-Ni metallic spherules interpreted as projectile impact melt droplets were reported from similar geologic contexts, namely from relatively small impact craters produced by metallic meteorites like Barringer Crater, Arizona, USA (e.g., Kelly et al., 1974; Mittlefehldt et al., 2005) and Whitecourt crater, Alberta, Canada (Kofman et al., 2010). Unfortunately, only limited petrographic information was provided. For this reason and because of the pristine petrographic and geochemical features of the Fe-Ni spherules from Kamil, our detailed mineralogical and geochemical work also offers a basis for discussing diagnostic criteria for the identification of impact spherules produced by iron projectiles hitting the Earth's crust. This is relevant for their discrimination from similar spherules of distinct origins that are described in the literature and for their correct interpretation. The most direct contrast is against metallic micrometeorites belonging to the I-type cosmic spherule group (Genge et al., 2008; Folco and Cordier, 2015) found at Earth's surface or in ancient sediments (e.g., Onoue et al., 2011; Dredge et al., 2010; Tomkins et al., 2016; Voldman et al., 2013; Suttle and Genge, 2017) and with ablation debris produced during the atmospheric flight of iron impactors like those recovered from the Sikhote Alin crater field, Russia (Badyukov and Rajtala, 2012).

2. Samples and methods

We studied a total of 28 spherules (Tables 1 and 2) by means of microanalytical field emission gun scanning electron microscope equipped with an energy dispersive system (FEG-SEM-EDS), electron probe microanalyzer (EPMA) and Raman spectroscopy analyses. The study population includes 25 Fe-Ni spherules: 23 Fe-Ni oxide spherules – the focus of the present paper, one Fe-Ni oxide-rich glassy spherule and one Fe-Ni metal spherule. The inclusion of the latter two spherules in the sample set was incidental. Both are covered by a shell of Fe-Ni oxides and could not be distinguished during our first selection, which was based on observations of the external surfaces under the SEM (see below). They, however, turned out relevant for the present work in documenting the variety of spherule types. One additional compound spherule (consisting of a glassy host spherule bearing an Fe-Ni

oxide bead) and two glass spherules with splashes of Fe-Ni oxide or metal materials on their external surfaces were – in turn deliberately – included in the study for their bearing on the definition of the oxide spherule formation mechanism. The two glass spherules belong to the population of impact glass spherules composed of the Kamil dark glass described in detail by Folco et al. (2015).

The spherules were selected from a batch of 135 particles recovered from four of the 44 soil samples (magnetic extraction < 5 mm) collected around the crater during our geophysical expedition in 2010 (see Folco et al., 2015, for details; Fig. 1). These spherules were spotted because of their typical metallic luster and hand-picked under a stereomicroscope and then positively identified through secondary electron and back-scattered electron imaging modes (SEI and BEI, respectively) of their external surfaces with a SEM Hitachi TM3030Plus Tabletop, equipped with a SwiftED3000 EDS system, at the Dipartimento di Scienze della Terra of the University of Pisa. Some BEI of the whole spherules collected during our survey were used in this paper to complete the description of the large varieties of structural and compositional features.

The search for oxide spherules was conducted on 13 soil samples collected along the NW-SE projectile trajectory established in previous works and mostly based on the asymmetric distribution of the ejecta (e.g., D'Orazio et al., 2011; Urbini et al., 2012). They include samples S11, S14, S15, S16, S40, S41, S42, S43, S44 and S23, S24, S25, S26 (labeled in yellow in Fig. 1), from the uprange and downrange areas of the crater, respectively. We choose soil samples from the downrange side of the crater for the expected greater abundance of microscopic impactor debris (according to Folco et al., 2015) and samples from the uprange side of the crater in the search for ablation spherules. Only the four downrange samples proved productive.

The selected spherules were first imaged under the FEG-SEM (both SEI and BEI modes) as whole specimens for detailed characterization of their morphology and external structure. They were then sectioned, polished and imaged under the FEG-SEM in order to define their internal texture, structure, mineral composition (Tables 1 and 2), and major element bulk composition (Table 3). Imaging and microanalytical FEG-SEM analyses were carried out at the Centro per la Integrazione della Strumentazione dell'Università di Pisa, using a FEI Quanta 450 ESEM-FEG equipped with a (EDS) Bruker QUANTAX energy dispersive system with a XFlash Detector 6|10. Bulk major element compositions (Table 3) were obtained by averaging two to five raster analyses (areas typically 30 by 30 μm in size), using the standard-less quantification method system. Running conditions were: 15 kV accelerating voltage, 10 mm working distance, nominal beam spot diameter $\sim 1 \mu\text{m}$.

The mineral chemistry of the various phases in the selected spherules (Fe-Ni oxides, Fe-rich silicate glass, Fe-Ni metal alloys, and silicate glasses) were obtained by EPMA at ISTERre, Grenoble, France, and at UNITECH - Piattaforme Tecnologiche di Ateneo, Dipartimento di Scienze della Terra, Università di Milano, Italy (Table 4). At ISTERre, we used a JEOL JXA8230 Superprobe. Running conditions were 15 kV accelerating voltage, 20 nA beam current, and 1 μm nominal beam spot. Raw data reduction was performed using the ZAF procedure. Reference materials (orthoclase, Cr-augite, chromite, VG2 and CCFA47 glasses) were repeatedly analyzed to check for instrumental drift and to correct measurements for deviation from recommended standard values. Detection limits (element wt%) are: 0.01% for Mg, Ca, K; 0.02 for Si, Fe, Al, Ti, P, Cr, S; 0.03 for Mn and Co; 0.04 for Na and Ni. At UNITECH, we used a JEOL Superprobe JXA8200. Running conditions were 15 kV accelerating voltage, 5 nA beam current, and 1 μm nominal beam spot. The PRZ data reduction method was used. The following standards were used for instrumental calibration: omphacite for Na, grossular for Al, Si, Ca, pyrite for Fe and S, rhodonite for Mn, K-feldspar for K, olivine for Mg, ilmenite for Ti, Y-phosphate for P, nickeline for Ni, and

Table 1
Main petrographic features of the Fe-Ni oxide and metal spherules from Kamil crater.

Label	Shape	Size (μm)	Mineral composition	Texture	External surface structure	Other surface features
Fe-Ni oxide spherule – Very high-Ni type						
S24 24	Spheroid	110	Ni-wüstite (80 vol.%) and trevorite (~20 vol.%)	Globular; grain size: 5 to 30 μm; few relatively large intergranular cavities towards particle center	Polygonal, bumpy	Scattered irregular cavities up to few tens of μm in size
Fe-Ni oxide spherules – High-Ni						
S24 L122	Spheroid	120	Trevorite (~73 vol.%) and minor interstitial	Symplectic; intergrowths of micrometer-sized dendrites; large rounded cavity at particle center	Graphic	One bulge of Fe-rich oxides 10 μm across Few welded angular bedrock fragments
S25 L10	Spheroid	130	Ni-wüstite (~27 vol.%; traces of Fe,Si,Al,P			
S24 L36	Spheroid	150	interstitial glass bearing nanoscopic			
S24 L177	Broken spheroid	150	Fe-Ni-Cu-P-rich nuggets			
Fe,Ni oxide spherules – Intermediate-Ni type						
S25 L31	Spheroid	270	Fe-trevorite or Ni-magnetite (86 vol%) and minor, interstitial Ni-wüstite (~24 vol.%; Ni-wüstite is more abundant towards particle center; traces of	Dendritic; grain size: ~20 μm; large (up to 1/3 of the spherule volume) rounded cavity at particle center	Boxwork, polygonal	Scattered welded angular bedrock fragments and silica glass patches Few silica rich glass patches Scattered welded angular bedrock fragments Scattered welded angular bedrock fragments
S25 L22	Spheroid	180	Fe-Si-Al-rich interstitial glass, bearing			
S24 L18.05	Spheroid	180	Fe-Ni-P-rich nanoscopic nuggets			
S24 L147	Spheroid	500				
S23 2	Broken spheroid	150				
S23 73	Spheroid	440				
S23 6	Spheroid	115				
S24 L31	Spheroid	270				
Fe,Ni oxide spherules – Intermediate-Ni type– Vitrophyric						
S23 L22	Spheroid	140	Fe-trevorite (~85 vol.%) in cryptocrystalline to glassy Fe-rich silicate matrix, bearing nanoscopic	Vitrophyric; grain size: 10–15 μm. Small scattered vesicles and irregular cavities up to few 10s of μm	Cantaloupe	Abundant adhering Si-Al glass patches and fragments Abundant adhering Si-Al glass patches and fragments Abundant adhering Si-Al glass patches and fragments
S23 L22	Spheroid	150	Fe-Ni-Cu-rich nuggets and microscopic Ni-wüstite grains in S24 L149 and S24 L216			
S24 L149	Spheroid	270				
S24 L82	Spheroid	190				
S24 L216	Ovoid	470				
Fe,Ni oxide spherules – Low-Ni type						
S25 L12	Spheroid	110	Ni-magnetite or Ni-bearing magnetite (85–90 vol.%) in emulsion P-bearing Fe-Si-rich matrix	Interlocking dendritic; grain size from 10 to 70 μm. Large rounded cavity at particle center and few vesicles	Gridded	Abundant adhering Si-Al glass patches and fragments
S25 L30	Spheroid	200				
S24 L153	Spheroid	280		Dendritic; grain size: ~10 μm; large central cavities and vesicles	Ashlar	Abundant adhering Si-Al glass patches and fragments Abundant adhering Si-Al glass patches and fragments
S25 L11	Spheroid	140				
S24 L40	Spheroid	195				
S23 77	Spheroid	180				
Fe,Ni oxide-rich glass spherule						
S23 L5	Spheroid	250	Ni-bearing wüstite (15 vol.%) and Ni-bearing magnetite (45 vol.%) in Fe-rich silicate glassy to cryptocrystalline matrix	Vitrophyric; grain size: 5–15 μm.	Boxwork, polygonal	Three welded angular bedrock fragments up to 100 μm in size
Metal spherule						
S24 L165	Spheroid	120	Fe,Ni metal globules (97 vol.%) in P-bearing sulfide matrix (EDS), with a shell of Fe-Ni oxides in a Fe-rich silicate matrix	Cellular; fine grained metallic cells (average cell size ~15 μm) with intergranular sulfide-rich matrix	Cantaloupe	Oxide shell speckled/laden with angular bedrock debris.

Table 2
Main petrographic features of compound spherule and splashes from Kamil crater.

Label	Type	Component	Compositional type	Shape	Size (μm)	Overall mineral composition	Texture	External surface texture
S23 76	Compound: oxide-rich glass spherule with protruding oxide bead	Bead Spherule	Very high-Ni	Spheroid Ovoid	50 270	Ni-wüstite (55 vol.%) and Fe-trevorite (~45 vol.%) Oxide rich domain: Ni-bearing magnetite (40 vol.%) in Fe-rich silicate glass matrix (60 vol.%) glass domain: vesicular Fe-rich glass	Globular, fine-grained (2 – 5 μm) Vitrophyric to glassy and vesiculated; large rounded cavity at particle center and few scattered vesicles Dendritic	Polygonal Dendritic, grading to vitreous
S23 L9	Splash: oxide splash on glass spherule	Splash Spherule	Very high-Ni	Splodge Spheroid	na 140	Ni-wüstite (95 vol.%) with traces of interstitial Fe-rich silica glass bearing few nanometric Fe-Ni-P-rich nuggets Fe-rich silicate glass	Glassy and highly vesicular Dendritic	Globular to feathered Featurreiss with scattered vesicles Rough to smooth and featurreiss
S24 L107	Splash: metal splash on glass spherule	Splash Spherule	High-Ni	Splodge Spheroid	na 120	Homogeneous Fe-Ni metal, partly oxidized Fe-rich silicate glass.	Featurreiss with rounded oxide spots Glassy and highly vesicular	Smooth and featurreiss with small scattered vesicles

Abbreviations: na = not applicable.

pure metals for Cr and Co. Detection limits (element wt%) are: 0.02 for Al, Mg, Si, Ca and K; 0.03 for Na, S, P, and 0.04 for Fe, Mn, Cr, Co and Ni. A test conducted on oxides from spherule S224 L122 to compare data from the two EPMA laboratories revealed concentration differences <1% relative for major elements and <10% relative for minor elements.

Iron concentration in Fe-Ni oxides and silicate glass was calculated assuming all iron as Fe^{2+} . Oxygen concentration was calculated by stoichiometry. For the studied Fe-Ni oxides, we considered analytical totals of $\sim 93 \pm 1$ wt% as indicative of Fe-Ni spinels of the magnetite ($\text{Fe}^{2+}\text{Fe}_3^{3+}\text{O}_4$) – trevorite ($\text{NiFe}_3^{3+}\text{O}_4$) series, as subsequently confirmed by Raman spectroscopy. Nickel-rich Fe-Ni-oxides with totals above ~ 96 wt% were taken to indicate Ni-Fe monoxides of the wüstite (FeO) – bunsenite (NiO) series. Such low totals may be in part explained by the nonstoichiometric composition of the monoxide ($\text{Ni, Fe}_{1-x}\text{O}$) (Luoma, 1995), in part because these Ni-rich oxides often contain Fe-Ni spinel exsolutions, as documented by combined FEG-SEM and Raman spectroscopy. In this paper we adopted the following nomenclature for the Fe-Ni spinels: trevorite for atomic $\text{Ni}/(\text{Ni} + \text{Fe}^{2+}) > 0.7$; Fe-trevorite for $\text{Ni}/(\text{Ni} + \text{Fe}^{2+})$ in the 0.5–0.7 range; Ni-magnetite for $\text{Ni}/(\text{Ni} + \text{Fe}^{2+})$ in the 0.1–0.5 range; Ni-bearing magnetite for $\text{Ni}/(\text{Ni} + \text{Fe}^{2+}) < 0.1$. For the Fe, Ni monoxides we used: bunsenite for $\text{Ni}/(\text{Ni} + \text{Fe}^{2+}) > 0.5$; Ni-wüstite for $\text{Ni}/(\text{Ni} + \text{Fe}^{2+})$ in the 0.1–0.5 range; Ni-bearing wüstite for $\text{Ni}/(\text{Ni} + \text{Fe}^{2+}) < 0.1$.

Unpolarized micro-Raman analyses were carried out on sectioned spherules for Fe-Ni oxide phase identification. Analyses were performed in nearly back-scattered geometry using a Jobin-Yvon Horiba XploRA Plus apparatus, at the Dipartimento di Scienze della Terra, University of Pisa, Italy. The instrument is equipped with a motorized x-y stage and an Olympus BX41 microscope with a $10 \times$ objective. A 532 nm light of a solid-state laser attenuated to 25% was employed. The minimum lateral and depth resolution was $\sim 1 \mu\text{m}$. The system was calibrated using the 520.6 cm^{-1} Raman band of silicon before, during and after each experimental session. Spectra were collected in multiple acquisition mode with single counting times of 60 s. Backscattered radiation was analyzed with a 600 mm^{-1} grating monochromator. Note that the high-Ni oxides with EPMA totals of ~ 96 wt% and interpreted in this paper as Ni-wüstite, provided Raman modes similar with that of trevorite (RRUFF R 140860), although slightly shifted towards higher wavelength number values in some cases. One possibility is that this Raman signal is due to the exsolved spinel phase, namely trevorite, and does not represent the host monoxide, Ni-wüstite. Resolving the fine relationships between the observed microstructural complexity in these exsolved Ni-rich oxides and their Raman effects needs further investigation, but is beyond the scope of the present paper.

3. Results

All 135 spherules studied here are highly magnetic, show a high degree of sphericity, are opaque and dark gray in color with a metallic luster. They were found abundantly in samples S23, S24, S25 and, less abundantly, in S26 from SE of the crater (Fig. 1), but not elsewhere, thereby documenting the virtual lack of spherules to the NW of the crater.

Main petrographic features of the Fe-Ni oxide and metal spherules are summarized in Table 1; those of the compound spherule and splashes in Table 2. Bulk major element composition by EDS analysis and mineral chemistry by EPMA are given in Tables 3 and 4, respectively.

3.1. Fe-Ni oxide spherules

A broad relationship between the bulk major element composition, namely the bulk $\text{Ni}/(\text{Ni} + \text{Fe})$ molar ratio, and external surface

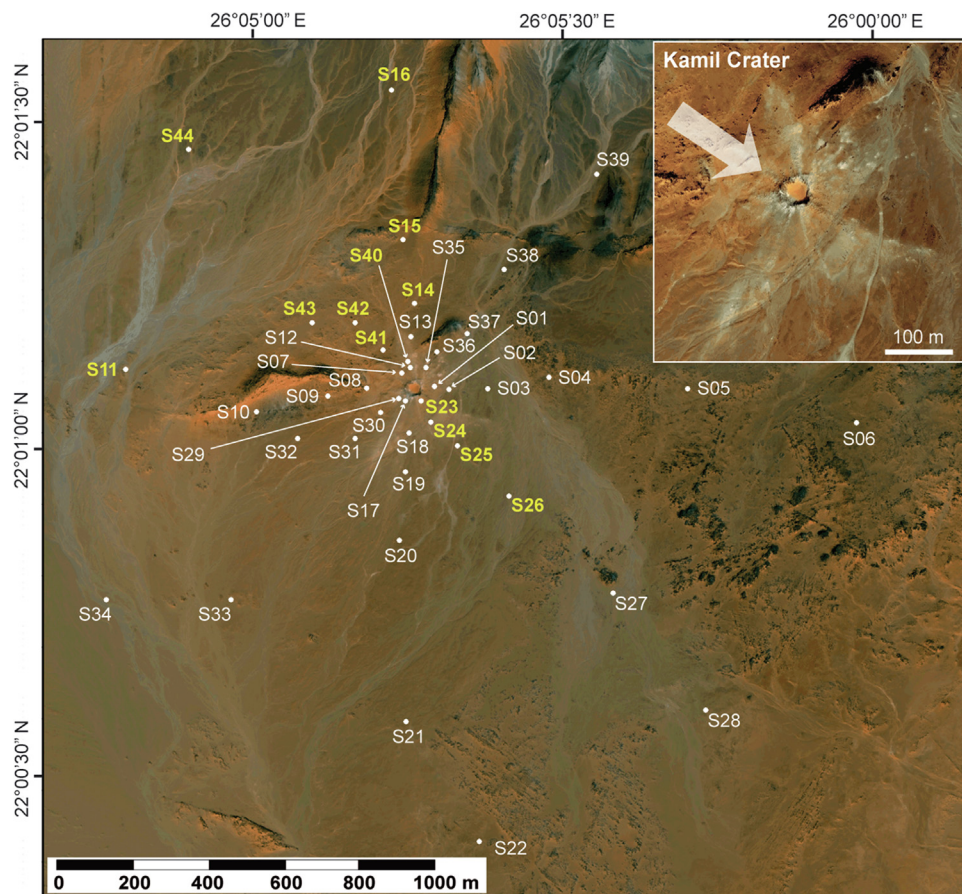


Fig. 1. Location map of the soil samples collected within an area of about 2.5×2.5 km around Kamil crater ($22^{\circ}01'06''\text{N}$, $26^{\circ}05'16''\text{E}$), southwestern Egypt, during our 2010 geophysical expedition (modified after Folco et al., 2015). Samples with yellow labels are the ones that were investigated for the extraction of Fe-Ni spherules studied in this work. Note that Fe-Ni spherules were only found in samples S23, S24, S25 and S26, from SE of the crater. Inset: Showing the approximate projectile incident direction, as inferred from ejecta distribution around the crater (D'Orazio et al. 2011; Urbini et al. 2012). Base map: enhanced true color QuickBird satellite image (22 October 2005; courtesy of Telespazio S.p.A.).

texture plus mineral composition observed in the Fe-Ni oxide spherules is the rationale for a compositional classification into the following types used in the paper: very high-Ni (~ 0.40), high-Ni (~ 0.30), intermediate-Ni (~ 0.20) and low-Ni types (< 0.1).

3.1.1. Very high-Ni type

S24 24 is the only individual spherule of this type in our selection (Fig. 2). It is an irregular spheroid $110 \mu\text{m}$ in diameter. In section, it shows globular texture given by nearly equiaxial grains 5 to $30 \mu\text{m}$ in size of Ni-wüstite, mantled by arrays of smaller subhedral trevorite grains. The cores of the Ni-wüstite grains bear nanometric-scale dendritic exsolution of trevorite (trunks and branches few tens of nm long/thick with cubic symmetry), whereas their margins abutting the surrounding trevorite are homogeneous. Submicroscopic intergranular cavities often occur at euhedral trevorite grain boundaries. Larger irregular cavities up to several tens of μm in size occur towards the center of the spherule and may extend to the external surface. The latter shows a bumpy, polygonal pattern, with Ni-wüstite globules in relief over the trevorite mantles, resembling, in places, “ribbed tomato” morphologies. The high Z-contrast dendritic patterns of the Ni-wüstite globules observed in BEI is a reflection of the fine exsolution intergrowths at their cores (compare Fig. 2B and 2D). Ni-wüstite and trevorite account for 80 and 20 vol.%, respectively.

The Ni/(Ni + Fe) molar ratios of the bulk spherule (Table 3), Ni-wüstite and trevorite (Table 4) are 0.40 , 0.49 and 0.30 , respectively.

The bulk spherule contains trace amounts of Si (Table 3); traces of Si, Al and P occur in trevorite (Table 4).

3.1.2. High-Ni type

We studied four spherules of this type: S24 L122, S25 L10, S24 L36 and S24 L177 (Fig. 3). They are nearly perfect spheres with diameters ranging from 120 to $150 \mu\text{m}$. One spherule, S24 L177, is a broken ovoid. In section, these spherules show symplectitic texture given by intergrowths of micrometer-sized dendrites of trevorite and Ni-wüstite, bearing fine trevorite exsolution as observed in the very high-Ni type spherule S24 24. While trevorite often shows subhedral to euhedral grain boundaries, Ni-wüstite exhibits anhedral shapes with interstitial setting. Traces of Fe-Si-Al \pm P interstitial glass, bearing nanoscale Fe-Ni-Cu-P-rich nuggets, completes the inventory of the observed mineral components (EDS identification; Fig. SM1). Trevorite and Ni-wüstite are often physically separated by submicroscopic intergranular cavities. Larger irregular cavities up to several tens of μm in size occur towards the center of the spherules. The external surfaces show graphic domain-structures with interstitial Ni-wüstite in relief. Trevorite and Ni-wüstite account for 75 and 25 vol.%, respectively. Spherule S24 L122 bears a bulge of fine-grained Fe-Ni oxides $\sim 5 \mu\text{m}$ in size (Fig. 3A). Spherules S25 L10 and S24 L177 bear bedrock debris welded to their surface or partially entrained, respectively (Table 1).

The Ni/(Ni + Fe) molar ratios of the bulk spherules (Table 3), trevorite and Ni-wüstite (Table 4) range from 0.30 to 0.35 , from 0.23

Table 3
Bulk composition (EDS; element wt% normalized to 100) of the Fe-Ni oxide and metal spherules from Kamil crater.

Label	Elements (wt%)	O	Al	Si	P	S	Fe	Ni	Ni/(Ni + Fe) mol
Fe-Ni oxide spherule – Very high-Ni type									
S24 24	Bulk	22.0	–	tr	–	–	45.6	32.4	0.40
Fe-Ni oxide spherules – High-Ni									
S24 L122	Bulk	22.2	–	0.5	0.2	–	51.5	25.7	0.32
S25 L10	Bulk	22.1	0.1	0.4	0.5	–	48.8	28.1	0.35
S24 L36	Bulk	22.6	–	tr	0.8	–	52.7	23.9	0.30
S24 L177	Bulk	22.3	–	0.5	–	–	51.2	26.0	0.33
Fe-Ni oxide spherules – Intermediate-Ni type – Dendritic									
S25 L31	Bulk	22.4	0.2	0.8	–	–	60.4	16.2	0.20
S25 L22	Bulk	22.0	–	–	–	–	63.1	14.9	0.18
S24 18.05	Bulk	22.1	–	–	–	–	64.7	13.0	0.17
S24 L147	Bulk	23.0	0.2	0.9	tr	–	61.7	14.0	0.18
S23 2	Bulk	22.2	–	tr	–	–	63.2	14.5	0.18
S23 73	Bulk	22.6	–	0.5	–	–	57.8	19.0	0.24
S23 6	Bulk	22.7	0.1	0.9	–	–	57.6	18.7	0.24
S24 L31	Bulk	23.0	0.2	1.2	tr	–	62.1	13.4	0.17
Fe-Ni oxide spherules – Intermediate-Ni type – Vitrophyric									
S23 L22	Bulk	24.4	0.5	3.2	–	–	58.5	13.4	0.18
S24 L149	Bulk	24.7	0.4	4.0	–	–	55.0	15.9	0.22
S24 L82	Bulk	26.4	0.5	6.3	0.2	–	53.4	13.2	0.19
S24 L216	Bulk	25.5	0.7	5.0	–	–	53.3	15.5	0.22
Fe-Ni oxide spherules – Low-Ni type									
S25 L12	Bulk	23.6	0.3	2.0	–	–	68.0	6.1	0.08
S25 L30	Bulk	22.7	0.1	0.6	tr	–	74.7	1.8	0.02
S24 L153	Bulk	25.0	0.3	3.6	0.3	–	68.7	2.1	0.03
S25 L11	Bulk	24.6	0.6	3.1	–	–	70.7	1.0	0.01
S24 L40	Bulk	23.3	0.2	1.2	tr	–	74.5	0.6	0.01
S23 77	Bulk	23.1	0.1	0.7	–	–	75.3	0.8	0.01
Fe-Ni oxide-rich glass spherule									
S23 L5	Bulk	28.8	1.7	8.4	tr	–	58.8	2.2	0.03
Metal spherule									
S24 L165	Bulk	–	–	–	0.7	1.3	75.2	22.8	0.22
Compound spherules									
S23 76	Bead	23.0	–	1.7	0.3	–	41.4	33.7	0.44
	Host	30.6	1.8	11.3	–	–	56.3	–	–
Splashes									
S23 L9	Splash	22.3	–	0.7	–	–	46.3	30.7	0.39
S24 L107	Splash	–	–	–	–	–	63.0	37.0	0.36

Abbreviations: tr = traces.

to 0.24 and from 0.39 to 0.43, respectively. The bulk spherule contains trace amounts of Si and P (Table 3); traces of Si, Al and P occur in both trevorite and Ni-wüstite (Table 4). The interstitial glass contains up to ~8 wt% Si and ~15 wt% P (Table 4).

3.1.3. Intermediate-Ni type

This group includes 12 spherules with similar Ni/(Ni + Fe) molar ratios and gradational petrographic properties between two end-member textural types: dendritic (Fig. 4) and vitrophyric (Fig. 5). S25 L31, S25 L22, S24 18.05, S24 L147, S23 2, S23 73, S23 6, S24 L31 belong to the former group, S23 L22, S24 L149, S24 L82, S24 L216 to the latter. Regardless of the subtype, they are nearly all perfect spheres with diameters ranging from 115 to 500 µm (Table 1); the only exception is S24 L216, which has an ovoid shape and a major axis of 490 µm.

The spherules of the subtype with dendritic texture (Fig. 4) are fine-grained with average grain size of 20 µm. They typically have one large rounded but not spherical, hollow cavity near the particle center, about 1/3 of the entire spherule volume (hollow spherules). Spherules mainly consist of dendrites of Fe-trevorite or Ni-magnetite (~85 vol.%) and minor interstitial Ni-wüstite

(~15 vol.%), plus traces of interstitial Fe-Si-rich glass, bearing Fe-Ni-P-rich nanoscale nuggets. Trevorite or Fe-trevorite may bear nanoscale exsolutions with high Z-contrast in BEI, most likely Ni-rich oxides (Fig. 4E). Iron-trevorite or Ni-magnetite and glass are more abundant towards the particle center. The external surface shows a boxwork structure given by networks of polygonal and pointed ridges of interstitial Ni-wüstite plus glass, enveloping cruciform dendrites of Fe-trevorite or Ni-magnetite up to a few tens of µm in size. Scattered angular fragments of bedrock debris are welded to the external surface of spherule S24 18.05 and S25 L31. Small patches of silica-rich glass are stuck onto the external surface of most of the spherules (Fig. 4B).

The Ni/(Ni + Fe) molar ratio of the bulk spherules (Table 3) ranges from 0.17 to 0.24, with an average value of 0.19 ± 0.03 . The Ni/(Ni + Fe) molar ratio in Fe-trevorite or Ni-magnetite and Ni-wüstite ranges from 0.15 to 0.20 and from 0.22 to 0.30, respectively (Table 4). The glass contains up to ~11 wt% Si, ~2 wt% P and traces of Al (Table 3). Silicon is detected in trace amounts in most of the analyzed oxides (Table 4).

The spherules of the vitrophyric subtype (Fig. 5) have distinctly higher abundance of Fe-rich silicate glass, up to ~15 vol.%. They

Table 4

Mineral composition (element wt%) of Fe-Ni oxide and metal spherules, compound spherule and splashes determined by EPMA (WDS) and SEM-EDS (EDS; normalized to 100 wt%). Iron concentration in Fe-Ni oxides calculated as Fe²⁺; oxygen concentration by stoichiometry. Compositions of the Gebel Kamil iron impactor and its mineral constituents, bedrock and impact melts from the literature (D'Orazio et al., 2011, and Fazio et al., 2016) are reported for comparison.

Spherule	Phase	Method	n	O	Na	Mg	Al	Si	P	S	K	Ca	Ti	Cr	Mn	Fe	Co	Ni	sum	Ni/Fe	Ni/Co	molar Ni/(Ni + Fe)
Fe-Ni oxide spherule – Very high-Ni type																						
S24 24	Ni-wüstite	WDS	5	20.9												36.1	1.19	37.2	95.4	1.030	31.3	0.49
	Trevorite	WDS	4	20.6			0.05	0.30	0.26							47.6	0.90	21.8	91.5	0.458	24.3	0.30
Fe,Ni oxide spherules – High-Ni type																						
S24 L122	Trevorite	WDS	7	20.6			0.15	0.17								53.6	0.67	17.2	92.3	0.320	25.8	0.23
	Ni-wüstite	WDS	8	21.2			0.04	0.22	0.03							43.7	1.16	29.3	95.5	0.690	25.3	0.39
S25 L10	Trevorite	WDS	3	20.4			0.09	0.07								53.5	0.54	17.4	92.1	0.325	32.3	0.24
	Ni-wüstite	WDS	3	21.2			0.04	0.06	0.04							43.1	1.14	30.8	96.4	0.716	27.1	0.41
S24 L36	Trevorite	WDS	3	20.3												54.3	0.59	16.9	92.1	0.312	28.9	0.23
	Ni-wüstite	WDS	3	21.1					0.04							43.4	1.05	30.5	96.0	0.704	29.0	0.40
	Matrix	EDS	1	33.9					14.7							46.9		4.5	99.9	0.095		0.08
S24 L177	Trevorite	WDS	3	20.4			0.07	0.09								53.0	0.60	17.8	92.0	0.336	29.6	0.24
	Ni-wüstite	WDS	3	21.1				0.05								41.3	1.15	32.5	96.2	0.788	28.6	0.43
	Matrix	EDS	1	30.3				7.6	3.4							52.2		6.3	99.9	0.122		0.10
Fe-Ni oxide spherules – Intermediate-Ni type																						
S25 L31	Fe-trevorite	WDS	5	20.8	0.04		0.09	0.05								57.0	0.51	15.0	93.5	0.264	29.3	0.20
	Ni-wüstite	WDS	4	21.7				0.08								55.3	1.03	19.8	97.9	0.358	19.2	0.25
	Matrix	EDS	1	31.5				10.9	1.70							52.0		3.9	100.0	0.074		0.07
S25 L22	Fe-trevorite	WDS	2	20.4												58.2	0.48	13.1	92.2	0.233	27.6	0.18
	Ni-wüstite	WDS	2	21.4												53.0	0.98	22.0	97.4	0.42	22.6	0.28
S24 18.05	Ni-magnetite	WDS	6	20.6				0.06								60.0	0.54	11.7	92.9	0.195	21.7	0.16
	Ni-wüstite	WDS	1	21.2		0.04										56.7	0.93	17.2	96.0	0.303	18.5	0.22
S24 L147	Fe-trevorite	WDS	3	20.5			0.15	0.23	0.03							55.6	0.49	14.7	91.7	0.264	30.3	0.20
	Matrix	EDS	1	30.2			0.3	8.8	1.8							54.4		4.5	100	0.082		0.07
S23 2	Fe-trevorite	WDS	5	20.6					0.07							56.8	0.45	15.0	92.8	0.264	33.7	0.20
	Ni-wüstite	WDS	5	21.1					0.06							50.6	0.68	23.2	95.8	0.459	35.5	0.30
S23 73	Ni-magnetite	WDS	2	20.8			0.04	0.36								59.9	0.45	11.1	92.7	0.185	24.7	0.15
	Ni-wüstite	WDS	9	21.3			0.03	0.43								54.2	0.67	18.5	95.1	0.342	28.0	0.24
S24 6	Fe-trevorite	WDS	1	20.6			0.08	0.09								56.9	0.55	14.4	92.6	0.254	26.6	0.19
	Ni-wüstite	WDS	4	22.4		0.03	0.07	1.69	0.17							52.8	0.75	17.5	95.5	0.332	23.2	0.24
S24 L31	Fe-trevorite	WDS	3	20.6			0.26	0.06								57.6	0.39	13.4	92.2	0.232	34.7	0.18
	Matrix	EDS	1	26.3			0.2	5.3	0.4							60.4		7.4	100.0	0.123		0.10
Fe-Ni oxide spherules – Intermediate-Ni type – Vitrophyric																						
S23 L22	Fe-trevorite	WDS	3	20.9			0.87	0.25								55.2	0.40	14.4	92.1	0.262	36.5	0.20
	Emulsion matrix	WDS		34.3	0.04	0.06	0.90	17.1	0.26		0.05	0.66	0.04		0.04	43.9	0.70	1.96	100.0	0.045	2.8	0.04
S24 L149	Fe-trevorite	WDS	5	21.0			0.60	0.23								55.4	0.55	14.9	92.7	0.269	27.4	0.20
	Ni-wüstite	WDS	3	23.3			0.14	2.01	0.04							51.5	1.07	20.7	98.8	0.403	19.3	0.28
	Emulsion matrix	WDS	2	32.3			0.21	15.3	0.35		0.03	0.19				44.1	0.93	4.33	97.8	0.098	4.7	0.08
S24 L82	Fe-trevorite	WDS	3	21.2			0.48	0.60								54.7	0.47	15.5	92.9	0.283	33.0	0.21
	Emulsion matrix	WDS	2	34.8			0.30	17.9	0.19			0.11				43.9	0.78	3.79	101.8	0.086	4.9	0.08
S24 L216	Fe-trevorite	WDS	3	21.9		0.03	1.27	0.93					0.09			54.5	0.59	14.1	93.5	0.259	24.0	0.20
	Ni-wüstite	WDS	3	21.9		0.03	0.25	0.42								44.5	1.15	29.7	98.0	0.667	25.7	0.39
	Emulsion matrix	WDS	1	34.4		0.08	0.54	17.1	0.29			0.16				43.4	1.07	4.38	101.4	0.101	4.1	0.09
Spherule	Phase	Method	n	O	Na	Mg	Al	Si	P	S	K	Ca	Ti	Cr	Mn	Fe	Co	Ni	sum	Ni/Fe	Ni/Co	molar Ni/(Ni + Fe)
Fe-Ni oxide spherules – Low-Ni type																						
S25 L12	Ni-magnetite	WDS	4	21.0			0.31	0.33								64.3	0.36	6.46	92.8	0.100	17.8	0.09
	Fe-Si glass matrix	WDS	3	27.6			0.39	8.84	0.41				0.14	0.11		55.4	0.25	1.88	95.0	0.034	7.5	0.03
S25 L30	Ni-magnetite	WDS	5	21.0			0.05	0.38	0.03							69.0	0.25	2.19	92.9	0.032	8.9	0.03
	Fe-Si glass matrix	EDS		27.4			0.06	7.2	0.44							63.7		1.12	100.0	0.018		0.02
S24 L153	Ni-magnetite	WDS	5	20.9			0.34	0.19								66.2	0.37	4.69	92.7	0.071	12.7	0.06

(continued on next page)

Table 4 (continued)

Spherule	Phase	Method	n	O	Na	Mg	Al	Si	P	S	K	Ca	Ti	Cr	Mn	Fe	Co	Ni	sum	Ni/Fe	Ni/Co	molar Ni/(Ni+Fe)
S25 L11	Fe-Si glass matrix	WDS	3	30.8			0.59	11.1	2.28			0.44	0.17		0.06	49.6	0.26	0.26	95.5	0.005	1.0	0.00
	Ni-bearing magnetite	WDS	3	21.4			0.55	0.55							0.05	69.2	0.15	1.16	93.0	0.017	7.5	0.02
S24 L40	Fe-Si glass matrix	WDS	4	29.5		0.03	1.04	10.6	0.75		0.04	0.39	0.20		0.10	52.6	0.14	0.09	95.4	0.002	0.6	0.00
	Ni-bearing magnetite	WDS	4	21.2			0.25	0.22							0.04	70.5	0.19	1.28	93.7	0.018	6.7	0.02
S23 77	Fe-Si glass matrix	WDS	3	26.0			0.27	6.00	0.87			0.11	0.08			61.2	0.14	0.45	95.2	0.007	3.3	0.01
	Ni-bearing magnetite	WDS	7	21.2		0.02	0.11	0.40					0.02	0.77	0.03	69.9		0.69	93.2	0.010		0.01
	Fe-Si glass matrix	WDS	10	23.9		0.03	0.09	4.44				0.02	0.03	0.20		64.6		0.37	93.70	0.006		0.01
Fe-Ni oxide-rich glass spherule																						
S23 L5	Ni-bearing wüstite	WDS	1	22.3			0.51	0.57			0.03		0.07			70.1	0.69	3.22	97.5	0.046	4.6	0.04
	Ni-bearing magnetite	WDS	4	22.5			2.26	1.04			0.08	0.02	0.15			64.4	0.41	2.20	93.1	0.034	5.3	0.03
	Fe-Si glass matrix	WDS	5	34.9	0.13	0.06	1.84	17.2	0.13		0.46	0.26	0.07		0.05	45.6	0.29	0.23	101.2	0.005	1.2	0.00
	Fe-Si glass matrix next to inclusion	WDS	1	35.0	0.51	0.04	4.14	15.8	0.06		0.68	0.80	0.05			43.2	0.34	0.41	101.0	0.009	1.2	0.01
	Fe-Si glass matrix next to fragment	WDS	1	36.1	0.06	0.12	4.92	16.7	0.10		0.60	0.22	0.14			41.9	0.27	0.26	101.3	0.006	1.0	0.01
	Porous fragment	WDS	1	43.9	0.23	0.40	18.4	21.0	0.03		0.60	0.33	1.35		0.05	7.2			93.4	0.000		0.00
Metal spherule																						
S24 L165	Fe-Ni metal	WDS	2						0.13							77.1	0.90	22.1	100.2	0.286	25.0	0.21
	Sulfide matrix	EDS	1							0.7	13.1					71.6		14.6	100.0	0.204		0.16
Compound spherules																						
S23 76	Ni-wüstite in bead	WDS	1	21.8			0.28	0.82	0.11				0.02			36.7	1.17	35.3	96.2	0.980	30.3	0.48
	Fe-trevorite in bead	WDS	1	21.1			1.07	0.59					0.12			54.4	0.41	13.3	91.0	0.245	32.1	0.19
	Ni-bearing magnetite in oxide-rich domain	WDS	3	24.3		0.03	1.29	4.62			0.02	0.07	0.17		0.05	60.3	0.06	1.43	92.3	0.024	24.7	0.02
	Fe-Si glass in oxide-rich domain	WDS	2	35.7		0.05	2.28	18.1	0.11			0.39	0.17			0.14	43.5	0.07	0.16	100.6	0.004	2.4
	Dark glass domain	WDS	1	40.2	0.45	0.14	7.76	21.4	0.10		0.19	0.33	0.45	0.02	0.60	26.3	0.12	1.74	99.7	0.066	14.8	0.06
Splashes																						
S23 L9	Ni-wüstite	WDS	1	21.2			0.09	0.08	0.03							38.6	1.08	35.3	96.4	0.914	32.6	0.47
	Dark glass	WDS	4	39.9		0.15	7.48	21.0	0.11		0.23	0.31	0.44		0.80	27.0	0.09	1.96	99.5	0.073	22.8	0.07
S24 L107	Fe-Ni metal	WDS	1	0.0					0.08							63.2	1.31	35.4	100.0	0.560	27.0	0.35
	Ni-bearing magnetite	EDS	1	22.6				0.30								74.7		1.7	100.0	0.023		0.02
	Dark glass	WDS	4	40.3		0.16	8.01	21.3	0.13		0.24	0.29	0.56		0.84	25.9	0.08	1.56	99.4	0.060	22.1	0.05
Spherule	Phase	Method	n	O	Na	Mg	Al	Si	P	S	K	Ca	Ti	Cr	Mn	Fe	Co	Ni	sum	Ni/Fe	Ni/Co	molar Ni/(Ni+Fe)
Gebel Kamil iron impactor																						
	Bulk metal	ICP-MS														78.6	0.76	20.6	100.0	0.26	27.1	0.20
	Kamacite	WDS				0.03	0.01									93.7	1.05	5.21	100.0	0.06	5.0	0.05
	Taenite	WDS				0.04										65.3	0.36	34.3	100.0	0.53	104	0.33
	Daubréelite	WDS						44.0					36.3			19.4			99.7			
	Schreibersite	WDS					15.0									50.4	0.18	34.6	100.2	0.69	197	0.40
	Schreibersite (high Ni)	WDS					15.0									32.3	0.07	52.5	99.9	1.62	780	0.61
	Troilite	WDS						36.3						0.06		63.5			101.3	0.00		
Bedrock																						
	Pale quartzarenite, negligible matrix contents	ICP-MS		53.4	0.04	0.11	0.13	46.7				0.04	0.04			0.08			100.5			
	Pale wacke with siltstone levels	ICP-MS		52.3	0.10	0.08	5.35	41.0	0.03	0.03	0.08	0.69				0.51			100.2			
	Reddish quartzarenite	ICP-MS		52.5	0.06	0.15	1.05	44.7	0.02			0.22	0.05	0.05	1.20				100.0			
Impact melt bombs/lapilli																						

Table 4 (continued)

Spherule	Phase	Method	n	O	Na	Mg	Al	Si	P	S	K	Ca	Ti	Cr	Mn	Fe	Co	Ni	sum	Ni/Fe	Ni/Co	molar Ni/(Ni+Fe)
White glass		XRF		52.6	0.07	0.18	0.93	45.0	0.01		0.03	0.24	0.09		0.02	0.60			99.7			
Dark glass		XRF		41.0		0.14	6.85	23.9	0.03	0.02	0.20	0.37	0.53		0.50	22.7	0.03	1.16	97.5	0.05	27.1	0.04
Impact melt glass spherules																						
Dark glass		WDS	108	40.7	0.0	0.1	6.7	23.1	0.1		0.2	0.4	0.5		0.6	24.0	0.1	2.0	98.5	0.09	23.7	0.08
		Std dev		1.3	0.0	0.0	1.6	1.9	0.1		0.1	0.1	0.1		0.2	3.2	0.1	1.1	1.2	0.04	12.8	0.03

consist of abundant Fe-trevorite (~85 vol.%) with cruciform skeletal habit in cryptocrystalline (as in S24 L82) to glassy (as in S23 L22) Fe-Si-rich matrix. The matrix includes nanoscale Fe-Ni-Cu-rich nuggets and, in S24 L149 and S24 L216, microscopic grains of Ni-wüstite. The cryptocrystalline matrix consists of nanoscale dendrites of Fe-Ni-rich oxides in silica-rich glass. Both the cryptocrystalline and glassy matrix may contain nanoscale cellular structures of Fe-Ni-rich blebs in silica-rich groundmass resembling emulsion textures often observed in impact melts (Hamann et al., 2018). The interface between trevorite microphe-nocrysts and matrix is often decorated by nanoscale arrays of interposed Ni-rich oxide grains and voids. The external surface exhibits a cantaloupe structural pattern. Scattered patches of silica-rich glass extending for a few tens of μm adhere to the surface of some spherules.

The Ni/(Ni + Fe) molar ratio of the bulk spherules (Table 3) ranges from 0.18 to 0.22, with an average value of 0.20 ± 0.02 , and thus it is indistinguishable from the dendritic spherule subtype. However, the Si and Al contents are higher, up to ~6 and ~1 wt%, respectively, accounting for the higher abundance of Fe-rich silicate glass. The Ni/(Ni + Fe) molar ratio in Fe-trevorite ranges from 0.20 to 0.21 (Table 4). Ni-wüstite grains in S24 L216 and S24 L149 have Ni/(Ni + Fe) ratio of 0.28 and 0.39, respectively. The glass contains up to 18 wt% Si, ~1 wt% Al, 0.35 wt% P and 0.66 wt% Ca \pm traces of Ti and Mg.

3.1.4. Low-Ni type

This group includes six spherules labeled S25 L12, S25 L30, S24 L153, S25 L11, S24 L40, and S23 77 (Fig. 6). The spherules have spherical shapes and diameters ranging from 110 to 280 μm . They have dendritic texture and are dominated (85–90 vol.%) by Ni-magnetite or Ni-bearing magnetite with cruciform habits set in matrix consisting of fine intergrowths of coalescent silica-rich and Fe-Ni-rich submicroscopic domains (with low and high Z-contrast in BEI) with vermicular to mottled texture, resembling quenched emulsions. Ni-magnetite or Ni-bearing magnetite cruciform dendrites are finely branched and elongated up to 70 μm in maximum dimension in S25 L12, S25 L30 and S24 L153, whereas they are nearly equiaxial and more fine-grained with an average grain size of 10 μm in S25 L11, S24 L40 and S23 77. Cavities of tens of μm with irregular or rounded shapes occur towards the center of the particles. The external surfaces of spherules S25 L12, S25 L30 and S24 L153 have gridded structure, whereas those of spherules S25 L11, S24 L40 and S23 77 have ashlar pattern, consistent with their internal textures. Some spherules have scattered patches of silica-rich glass extending for a few tens of μm adhering to their external surfaces.

The Ni/(Ni + Fe) molar ratio of the bulk spherules (Table 3) ranges from 0.01 to 0.08, with an average value of 0.03 ± 0.03 . Silicon content ranges from ~1 to ~4 wt%. Aluminum is present in detectable amounts, although always < 1 wt%. The average Ni/(Ni + Fe) molar ratio in Ni-magnetite or Ni-bearing magnetite is 0.04 ± 0.03 and ranges from 0.01 to 0.09 (Table 4). Silicon is detected in trace to minor amounts in most of the analyzed oxides (Table 4). In the bulk matrix, Si ranges from 4.4 to 11.1 wt%, Al from 0.09 to 1.4, P from 0.44 to 2.28, Fe from 49.9 to 64.6 and Ni from 0.5 to 1.9 (Table 4).

3.2. The Fe-Ni oxide-rich glass spherule

S23 L5 is the only individual spherule of this type in our selection (Fig. 7). It has a spheroid shape with a diameter of 250 μm . Three large angular to subangular bedrock fragments are stuck onto its external surface. Several smaller masses of vesicular silica glass are partly embedded in the host spherule. The sectioned

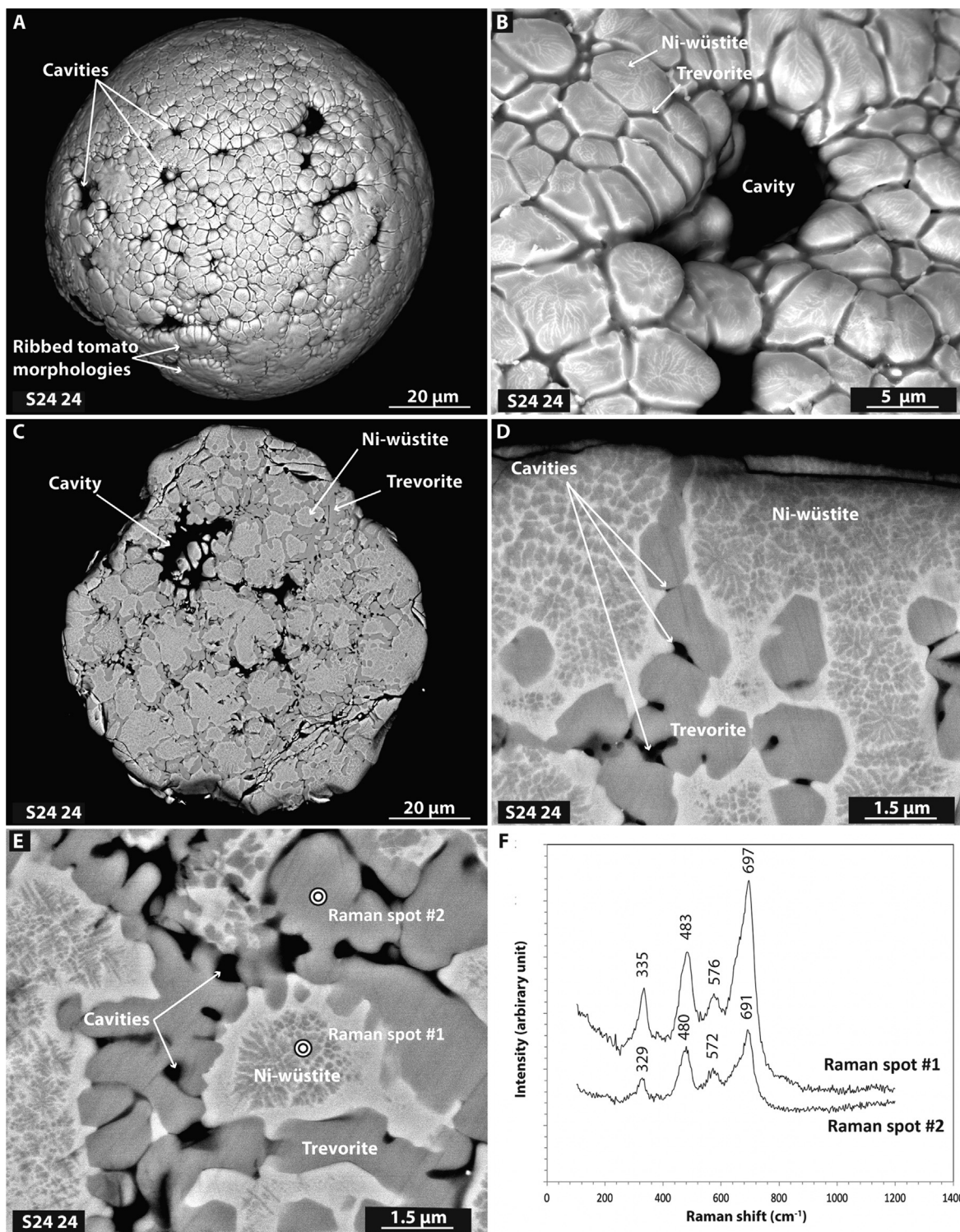


Fig. 2. Iron-Ni oxide spherule S24 24 of the very high-Ni compositional type (A to E: BEI; F: Raman spectra). A) Whole spherule showing bumpy polygonal surface structure with, in places, ribbed tomato shapes (arrowed), and irregular cavities, up to a few 10s of μm across. B) A close-up view of the surface structure: rounded polygons of Ni-wüstite in relief over surrounding trevorite, and irregular cavities. The dendritic patterns for the Ni-wüstite cores are the reflection of nanoscale intergrowths of exsolved trevorite. C) Section of the spherule showing globular texture. D) Textural details of Ni-wüstite globules with the surrounding subhedral trevorite. Ni-wüstite exhibits finely-exsolved cores and homogeneous rims. Submicroscopic intergranular cavities are arrowed. E) Raman spectra location map. Note, also, the cubic symmetry of the dendritic exsolutions of trevorite in Ni-wüstite. F) Raman spectra of exsolved Ni-wüstite-trevorite cores (#1) and trevorite (#2).

spherule shows a vitrophyric texture with finely branched dendrites of Ni-bearing wüstite and Ni-bearing magnetite, 5 to 15 μm in size, set in a glassy to cryptocrystalline Fe-rich silicate matrix. Abundances for Ni-bearing wüstite, Ni-bearing magnetite

and glass are 15, 45, 30 vol.%, respectively. Ni-bearing wüstite dominates the core of the spherule; Ni-bearing magnetite the outer regions and forms a nearly continuous surface shell. The latter feature makes this type of particle nearly indistinguishable from the

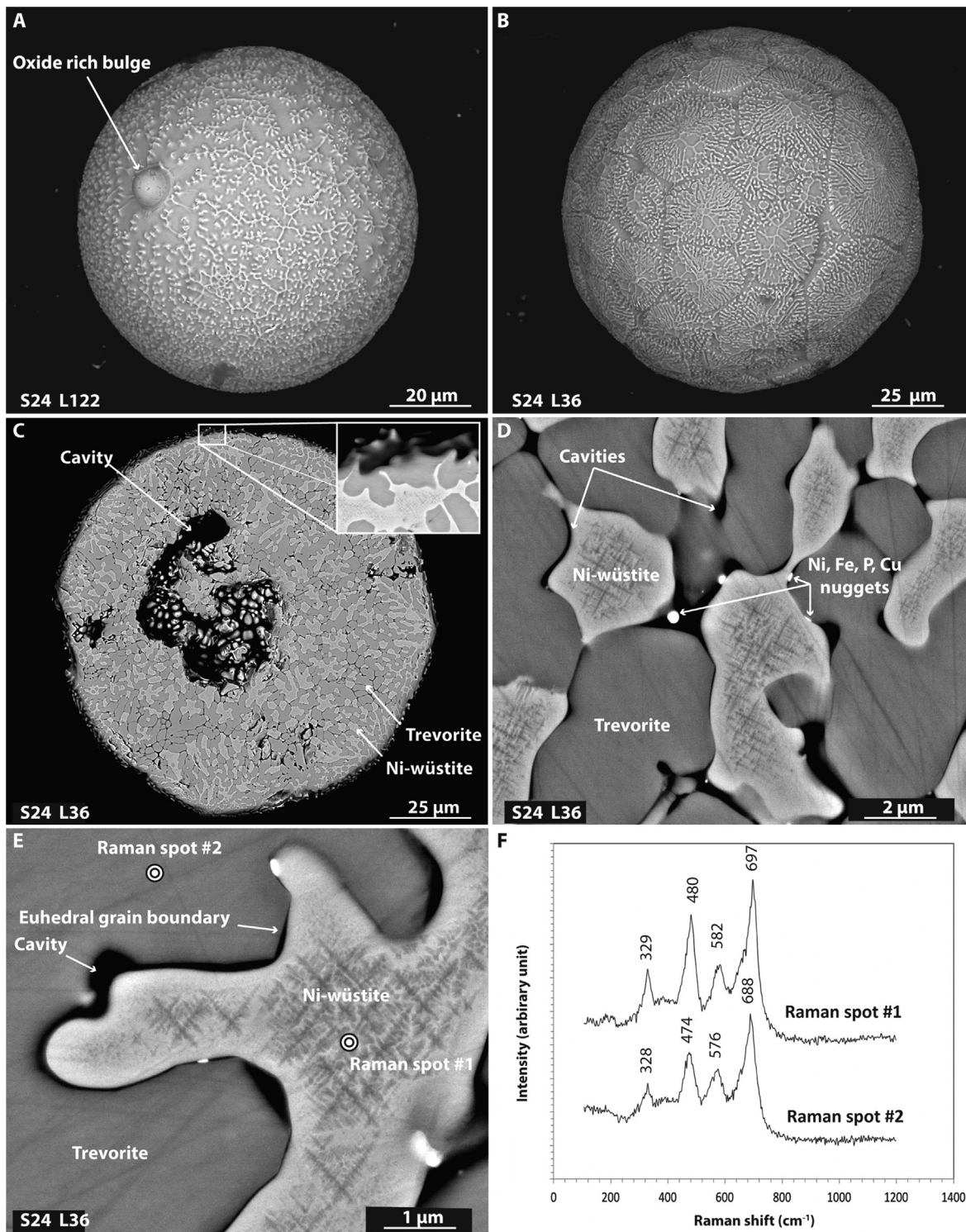


Fig. 3. Iron-Ni oxide spherules of the very high-Ni compositional type (A to E: BEI; F: Raman spectra). A and B) Spherules S24 L122 and S24 L36 showing graphic surface structure resulting from fine trevorite – Ni-wüstite intergrowth. The high Z-contrast vermicular features in relief consists of Ni-wüstite. C) Section of the spherule S24 L36 showing trevorite – Ni-wüstite symplectitic texture. Nickel-wüstite cores bear nanoscale exsolution of trevorite. Note the large irregular cavity up to several tens of μm in size near the particle center. Inset: showing Ni-wüstite forming the vermicular features on the external surface in relief. D) Textural details of the trevorite – Ni-wüstite intergrowths in spherule S24 L36. Note the fine trevorite exsolution at the cores of Ni-wüstite grains, the intergranular cavities and the interstitial metallic nuggets. E) Raman spectra location map for spherule S24 L36. Note, also, the euhedral grain boundaries of trevorite. F) Raman spectra of exsolved Ni-wüstite-trevorite cores (#1) and trevorite (#2) in S24 L36.

oxide spheres (described in Chapter 3.1) based on examination of the external surface only. A composite glass inclusion about $40\ \mu\text{m}$ across occurs at the margin of the particle and is dominated by silica glass. The largest of the three bedrock fragments stuck to

the spherule surface is sampled by the section. It is a porous, clastic aggregate of fine-grained minerals and rock fragments consisting mainly of platy minerals, likely clay, and quartz. The fragment is welded to the host spherule by a film of vesicular glass virtually

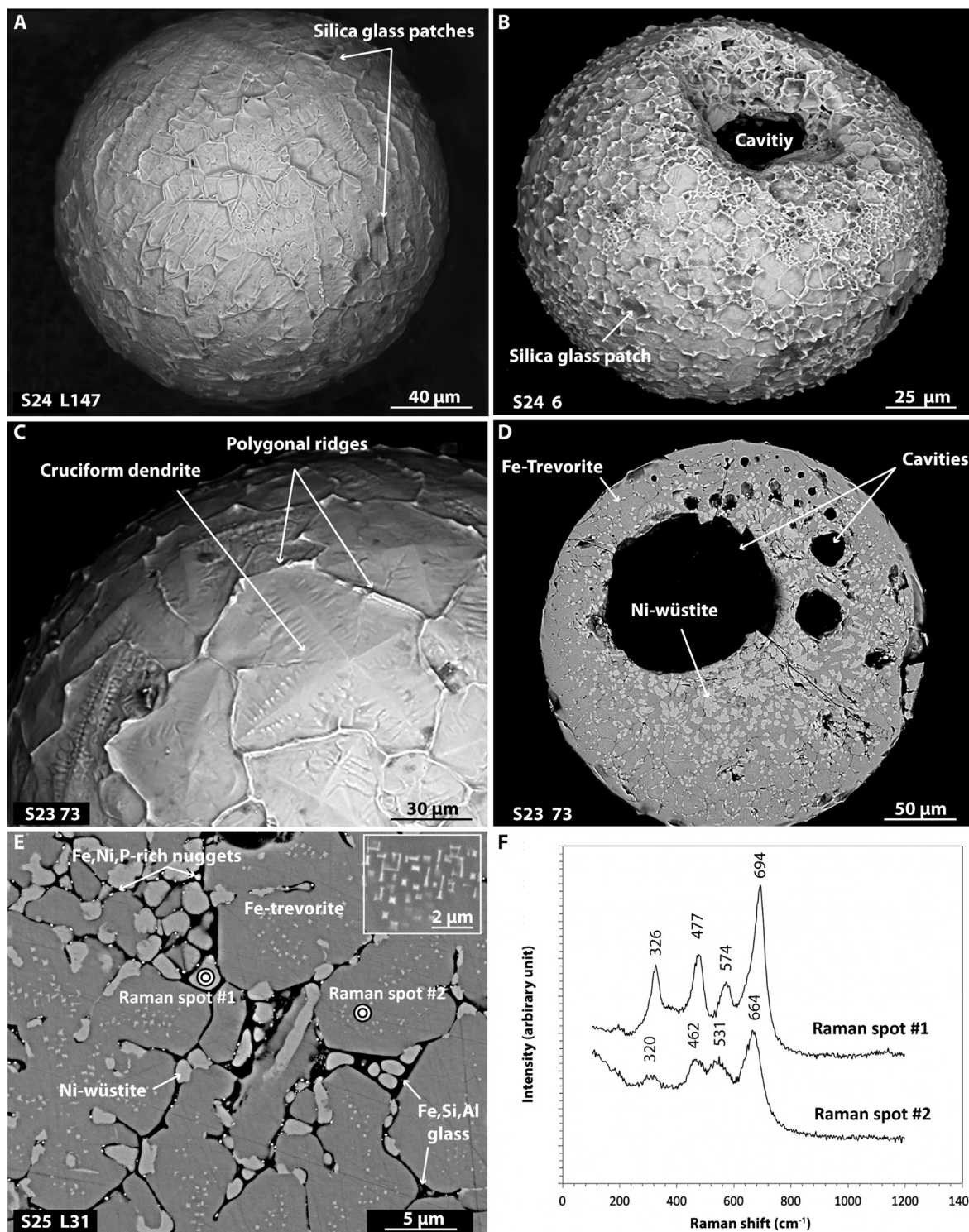


Fig. 4. Iron-Ni oxide spherules of the intermediate-Ni compositional type (A to E: BEI; F: Raman spectra). A and B) Spherules S24 L147 and S24 6 showing boxwork surface structure. Note the hollow structure of spherule S24 6. C) A close-up view of the boxwork structure of spherule S23 73 given by a network of polygonal, ridges of interstitial material (arrowed) enveloping low-relief cruciform dendrites of Fe-trevorite (arrowed). D) Section of spherule S23 73 dominated by dendrites of Fe-trevorite with minor interstitial trevorite. Note that the Fe-trevorite/trevorite volume ratio decreases towards the center of the spherule. E) Raman spectra location map for spherule S25 L31. Note also the fine exsolutions with cubic structural pattern in Fe-trevorite (inset), the interstitial setting of trevorite and Fe-Si-Al-rich interstitial glass. F) Raman spectra of Ni-wüstite (#1) and trevorite (#2) in spherule S25 L31.

devoid of Fe-Ni oxides. A petrographically similar glass layer is observed around the inclusion. Few round cavities up to few tens of μm across occur inside the spherule. The external surface of the Ni-magnetite surface shell described above shows polygonal boxwork structure.

The Ni/(Ni + Fe) molar ratio of the bulk spherule (Table 3) is low, namely 0.03, and similar to that of Ni-bearing wüstite, 0.04, and Ni-bearing magnetite, 0.03 (Table 4). Silicon is detected in minor amounts in the analyzed oxides (Table 4). Glass contains abundant Fe = 45.6 wt% and Si = 17.2 wt% and minor Al = 1.84 wt% and traces

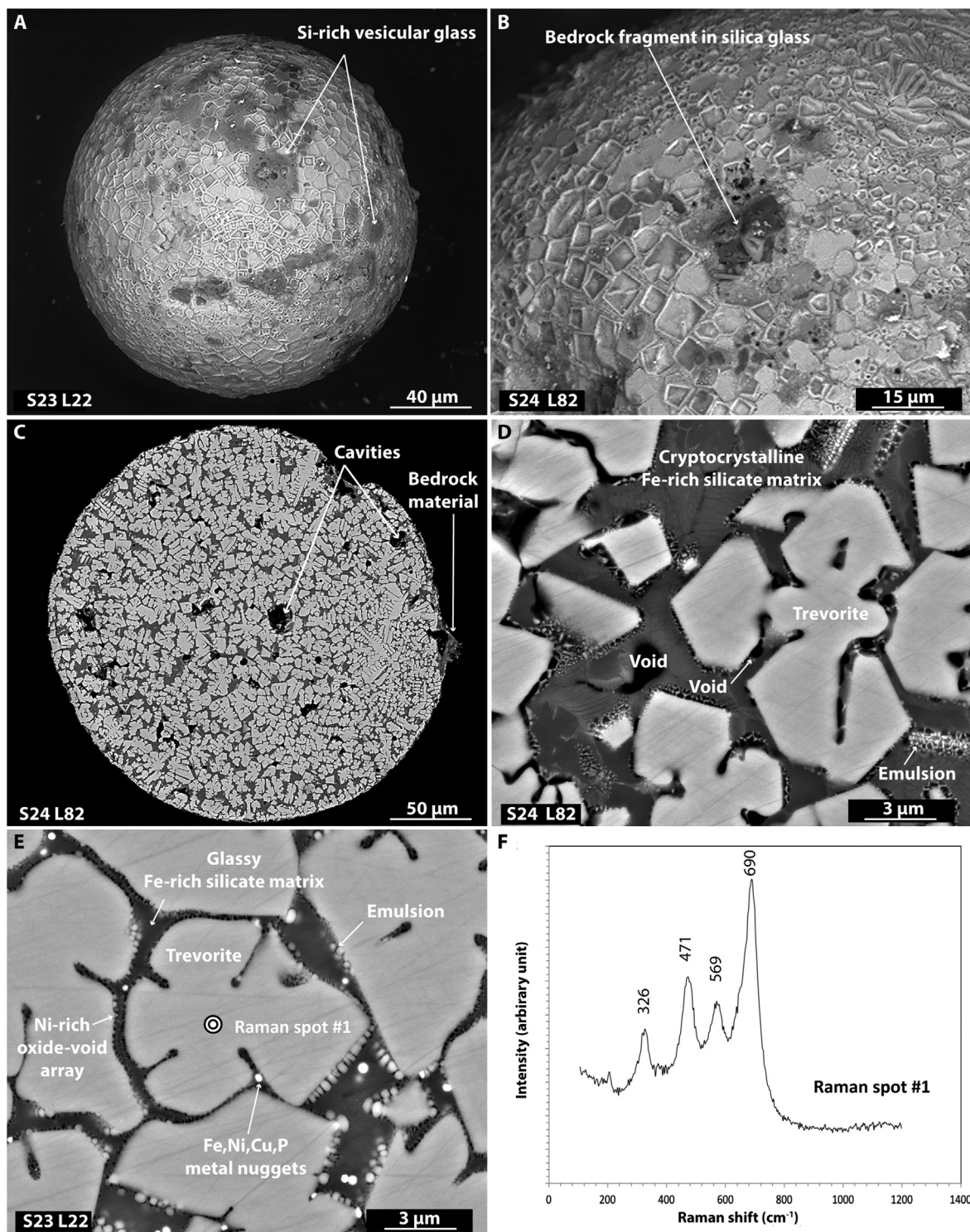


Fig. 5. Vitrophyric Fe-Ni oxide spherules of the intermediate-Ni compositional type. (A to E: BEI; F: Raman spectrum). A) Spherule S23 L22 showing cantaloupe surface structure and scattered patches of silica-rich glass. B) A close-up view of the cantaloupe surface structure in spherule S24 L82. C) Section of S24 L82 spherule showing vitrophyric texture and consisting of trevorite set in cryptocrystalline matrix. D) A close-up view of a section of spherule S24 L82 showing the cruciform habit of trevorite crystals, the nanoscale dendrites (cryptocrystals) of Fe-Ni-rich oxides in silica-rich glass, and the nanoscale emulsions. E) Raman spectra location map for spherule S23 L22. Note also the Fe-Ni-Cu-rich nuggets set in the glass matrix and the nanoscale arrays of interposed Ni-rich oxide grains and voids lining trevorite crystal boundaries. F) Raman spectrum of trevorite (#1) in spherule S23 L22.

of Ni = 0.23 wt% and P = 0.13 wt%. The glassy inclusion consists of nearly pure SiO_2 , i.e. lechatelierite (EDS identification) and the bedrock fragment on the surface is composed mainly of Si, Al and minor Fe and Ti, consistent with a clay plus quartz aggregate composition.

3.3. The Fe-Ni metal spherule

S24 L165 is the only individual spherule of this type in our selection (Fig. 8). With a spheroid shape and a diameter of 120 μm it is mainly composed by a Fe-Ni metal alloy plus minor

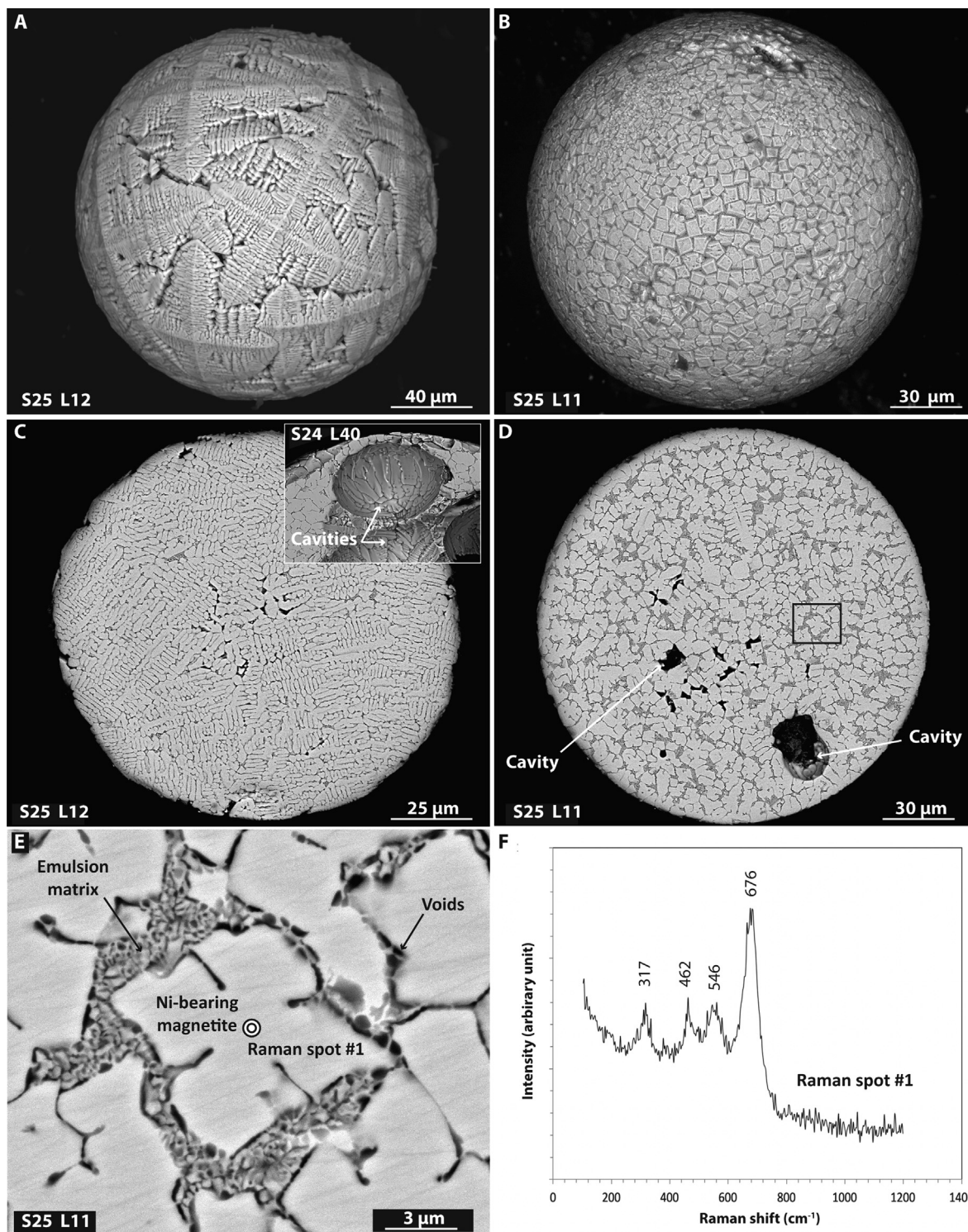


Fig. 6. Fe-Ni oxide spherules of the low-Ni compositional type (A to E: BEI; F: Raman spectrum). A) Spherule S25 L12 showing gridded surface structure given by finely branched, cruciform dendrites of Ni-magnetite. B) Spherule S25 L11 showing ashlar surface structure given by equiaxial Ni-bearing magnetite grains in relief. C) Section of spherule S25 L12 showing branched dendritic texture. Inset: a portion of a section of spherule S24 L40 showing large round cavities. D) Section of spherule S25 L11 exhibiting nearly equiaxial Ni-bearing magnetite dendrites. E) Raman spectra location map for spherule S25 L11. Note the fine intergrowth of Si-rich and Fe-rich (dark and bright Z-contrasts, respectively) materials composing the matrix. They likely are emulsions. F) Raman spectrum of Ni-bearing magnetite (#1) in spherule S25 L11.

sulfides, enveloped by a thin shell of Fe-Ni oxides plus minor Fe-rich silicate glass a few μm thick. This particle type is thus indistinguishable from the oxide spheres based on examination of the external surface only. In section, the Fe-Ni metal alloy shows globular texture with equigranular cells up to $\sim 10 \mu\text{m}$ wide. Interstitial

sulfide-rich matrix accounts for about 3 vol.%. Irregularly shaped cavities up to a few tens of μm across occur at the center of the spherule. Unfortunately, part of the thin shell was lost during sectioning and we have little textural information; however, the external surface reveals a cantaloupe structure typical of the

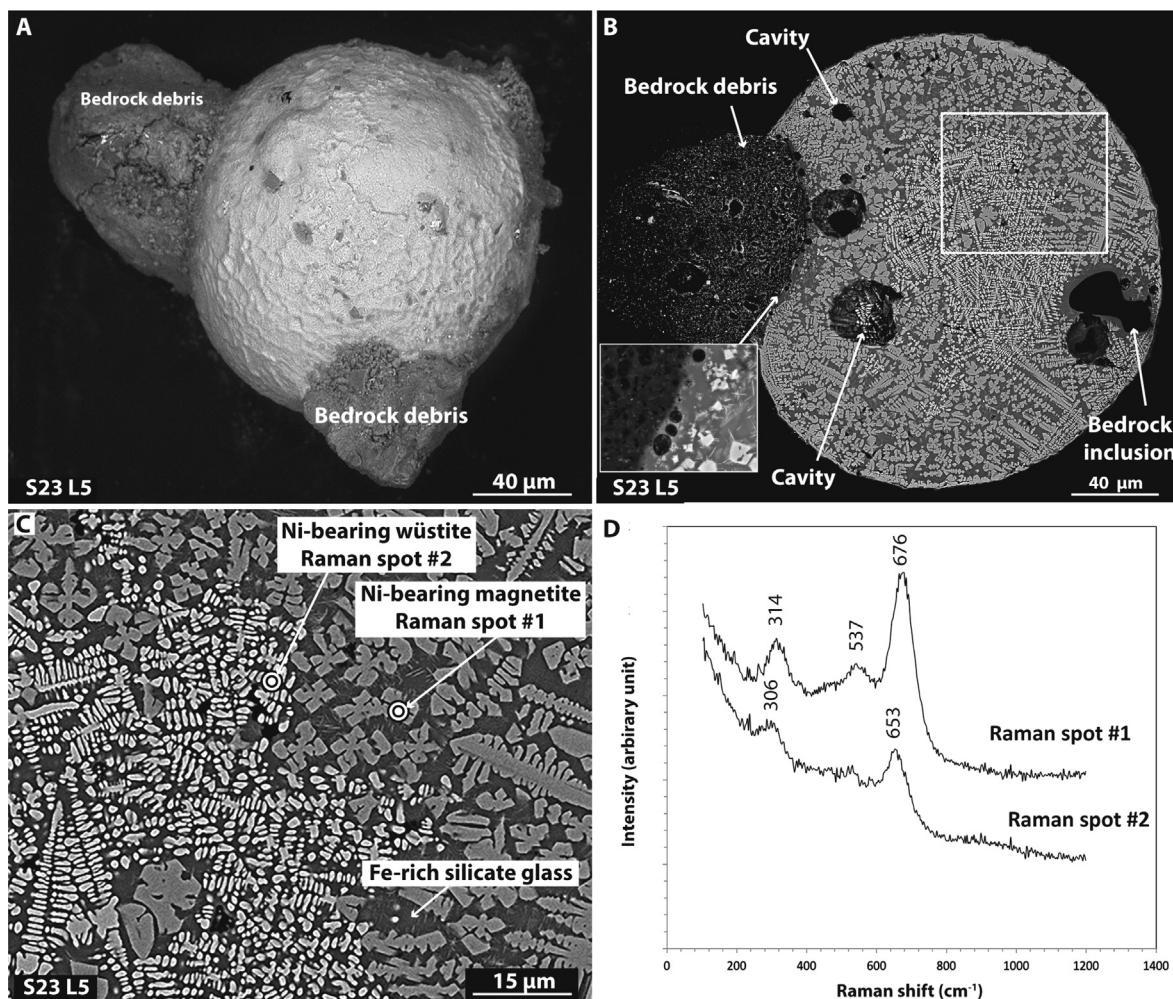


Fig. 7. Fe-Ni oxide-rich glass sphere S23 L5 (A to C: BEI; D: Raman spectra). A) Whole spherule showing polygonal boxwork surface structure. Three bedrock fragments several tens of μm in size are stuck to its surface. B) Sectioned particle showing vitrophyric texture given by microdendrites of Ni-wüstite (mainly at particle center) and Ni-magnetite set in glassy to cryptocrystalline matrix of Fe-rich silicate glass. Lechatelierite inclusion, vesicles and bedrock fragments are arrowed. The white rectangle outlines the area of the section featured in panel C. Inset: detail of the fragment – spherule contact showing welding due to vesicular silicate glass. C) Raman spectra location map. D) Raman spectra of Ni-bearing magnetite (#1) and Ni-bearing wüstite (#2).

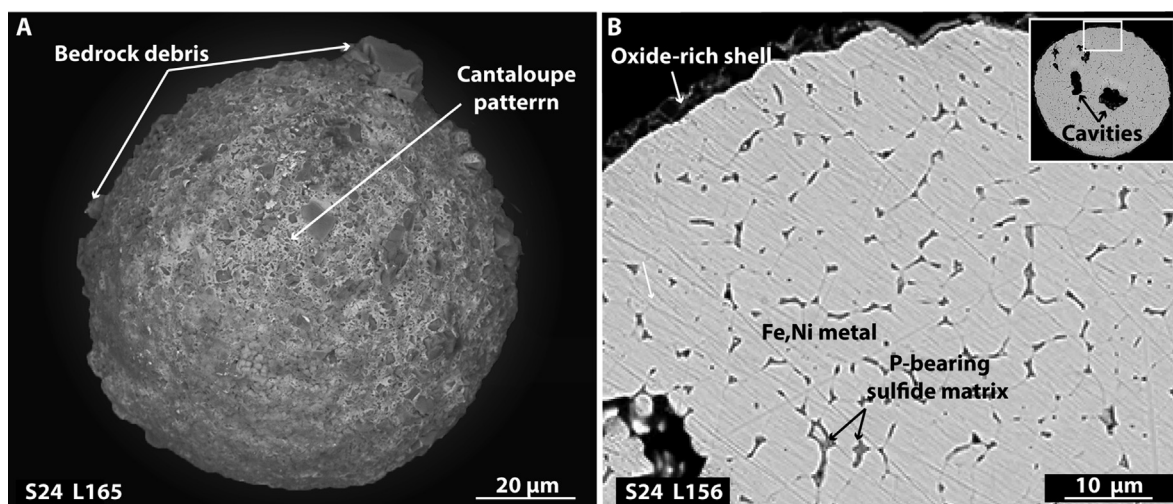


Fig. 8. Fe-Ni metal spherule S24 L165 (A and B: BEI). A) Whole spherule showing a crumble crust texture due to abundant bedrock fragments stuck onto its surface. The primary structure of the external surface of the spherule shows the cantaloupe pattern of the Fe-Ni-oxide rich shell (arrowed). B) A detail of the sectioned particle showing the metal core and the oxide-rich thin shell (arrowed). The metal core consists of fine-grained globular Fe-Ni metal alloy globules with minor P-bearing sulfide rich interstitial matrix. Inset: location map; central cavities are arrowed.

vitrophyric oxide spherules (see above). Overall, the external surface has a crumble crust texture as it is speckled with fine bedrock debris (mainly quartz and wacke fragments).

The Ni/(Ni + Fe) molar ratio of the bulk metal spherule is 0.22 (Table 3) similar to that of the intermediate-Ni type Fe-Ni oxide spherules. The Ni/(Ni + Fe) molar ratio of the metal phase is 0.21 (Table 4). This value is similar to the bulk value, consistently with the fact that the spherule is dominated by metal. The sulfide matrix is dominated by Fe = 71.6 wt%, Ni = 14.6 wt% and S = 13.1 wt% with minor amounts of P = 0.7 wt% (Table 4).

3.4. Compound spherules

Particle S23 76 is the only individual spherule of this type in our selection (Fig. 9). It consists of two conjoined spherules, namely, a larger glassy spherule hosting a smaller oxide bead. The glassy spherule is actually a spheroid with an ovoid shape and maximum elongation of 270 μm . The oxide bead has spherical shape and is 50 μm in diameter. It partly protrudes from the surface of the host, through one of its tips. Whole-specimen observations reveal that the glassy spherule is dominated by vesicular glass on one side (Fig. 9A); then, the composition gradually changes moving towards the oxide bead, with a progressive increase of fine-grained dendritic oxides. The spherule was sectioned twice to intercept its three components. Through the first section (not shown here) we could investigate the glass domain of the host spherule, which consists of featureless, yet vesiculated, Fe-rich silicate glass. Through the second section (Fig. 9B and 9C) we could investigate the oxide-rich domain of the host glass spherule and the oxide bead. The oxide-rich region is vitrophyric and consists of cruciform, finely branched, microscopic dendrites of Ni-bearing magnetite set in a glassy to cryptocrystalline Fe-rich silicate matrix. A large, round, hollow cavity (~60 μm in diameter) occurs near the center of the host spherule, along with some smaller vesicles. The bead shows a globular texture given by nearly equant grains, 2 to 5 μm in size, of Ni-wüstite mantled by arrays of smaller subhedral Fe-trevorite grains. The cores of the Ni-wüstite grains bear nanoscale exsolutions of Fe-trevorite. Submicroscopic intergranular cavities often occur at grain boundaries. Fe-trevorite grains line the contact with the host spherule and finely extend into the host spherule glass. The external surface structure varies from vitreous, to dendritic, to polygonal, moving from the glassy domain of the host glass spherule, through its oxide-rich region, to the bead. A close inspection of the contact reveals that the glass of the host spherule wets the bead.

The Ni/(Ni + Fe) molar ratio of the bulk oxide rich domain of the host glass spherule and bead are 0 and 0.44, respectively (Table 3). The bulk bead contains minor amounts of Si and trace amounts of P. The Fe content in the Fe-rich silicate glass of the host spherule increases significantly from the glass (oxide-free) domain, 26.3 wt%, to the oxide-rich domain, 43.5 wt%, whereas Si and Al decrease from 21.4 to 18.1 wt%, and from 7.76 to 2.28 wt%, respectively (Table 4). The Ni/(Ni + Fe) molar ratio in Ni-bearing magnetite (in the host spherule), Fe-trevorite and Ni-wüstite (in the bead) are 0.02, 0.19 and 0.48, respectively. The relatively high Si and Al contents in Ni-bearing magnetite are likely artifacts, namely matrix contamination in the spot analyses due to the small size of the oxide grains relative to excitation volume of the EMPA electron beam.

For the discussion below, note the striking textural and compositional similarity between the oxide bead and the Fe-Ni oxide spherule S24 24, the oxide rich region and the oxide-rich glass spherule S23 L5. Also, the composition and vesicularity of the glass region are indistinguishable from those of the Kamil dark (impactor-rich) glass (Table 4).

3.5. Splashes on impact glass spherules

S23 L09 and S24 L107 are two impact spherules of Kamil dark glass with splashes of Fe-Ni oxide or metal material on their external surfaces (Fig. 10). Spherule S23 L09 bears two splashes on two opposite sides in the form of caps with central mounds. Altogether, the particle has an ovoid shape with maximum elongation of 140 μm . The two caps extend from the central mound over a total of about half of the host glass spherule through aprons and streamlets. Their external surface is rough with feathered structure at the central mounds and smooth and featureless at the aprons and streamlets. The external surface of the host glass spherule is smooth and vesicular. In places, streamlets and aprons cover vesicles; vice versa, they are cut by vesicles in others, indicating venting of the substrate at the time of the emplacement.

The section reveals that the host spherule consists of highly vesicular Fe-rich silicate glass. The oxide splashes are dominated by microscopic, closely packed dendrites of Ni-wüstite (~95 vol. %) with traces of interstitial Fe-rich silica glass. Nickel-wüstite contains nanoscale exsolutions. The glass includes a few nanometric Fe-Ni-P-Cu-rich nuggets. The contact between the oxide splashes and the host is either neat and follows the spherical morphology of the host spherule, or embayed, disrupting the spherical morphology of the host spherule (Fig. 10B); at a closer look, the latter is finely digitated with elongated Ni-wüstite dendrites extending into the host glass for a few μm (Fig. 10C). Here the glass shows a brighter Z-contrast suggesting higher Fe concentrations as in diffusion boundary layers.

The Ni/(Ni + Fe) molar ratio of the bulk oxide splash and Ni-wüstite are 0.39 and 0.47, respectively (Table 3). The bulk oxide splash contains minor amounts of Si, 1.7 wt%, and traces of P, 0.03 wt% (Table 4); Ni-wüstite contains trace amounts of Si, Al and P, 0.08, 0.09 and 0.03 wt%, respectively. The silicate glass composing the host spherule shows element concentrations within the variability of the published Kamil dark glass, with abundant Fe and Al, 27 and 7.48 wt%, respectively, and a low Ni/(Ni + Fe) molar ratio of 0.07 (Table 4).

Spherule S24 L107 is very similar to spherule S23 L09 but the splash consists of a cap of Fe-Ni metal alloy topped by an oxidized layer. In section the metal is featureless with oxidized spots. The glass of Fe-rich silicate composition is highly vesicular. A diffusion band is observed in the glass at the contact with the metal splash and decorated by nanometric dendrites of Fe-Ni rich oxides which grow perpendicular to the contact (Fig. 10D).

The Ni/(Ni + Fe) molar ratio of the bulk metal splash is 0.36 (Table 3). The silicate glass of the host spherule contains abundant Fe and Al, 25.9 and 8.01 wt%, respectively, with low Ni/(Ni + Fe) molar ratio of 0.05 (Table 4); overall its composition overlaps that of the Kamil dark glass.

4. Discussion

4.1. Mineralogical and textural evolution of the Fe-Ni oxide and metal spherules

The Fe-Ni oxide spherules from Kamil crater show a large variety of textures and compositions. The occurrence of one metal spherule and one metal splash adds to the inventory of Fe-Ni spherules and attests to formation under varying oxygen activity. High sphericity, dendritic textures and mineral compositions dominated by either Fe-Ni oxides or homogenous Fe-Ni metal indicate formation through quenching of high temperature (>1600–1500 °C; Raghavan, 2010; Yang et al., 1996; see below) oxide or metal liquid droplets.

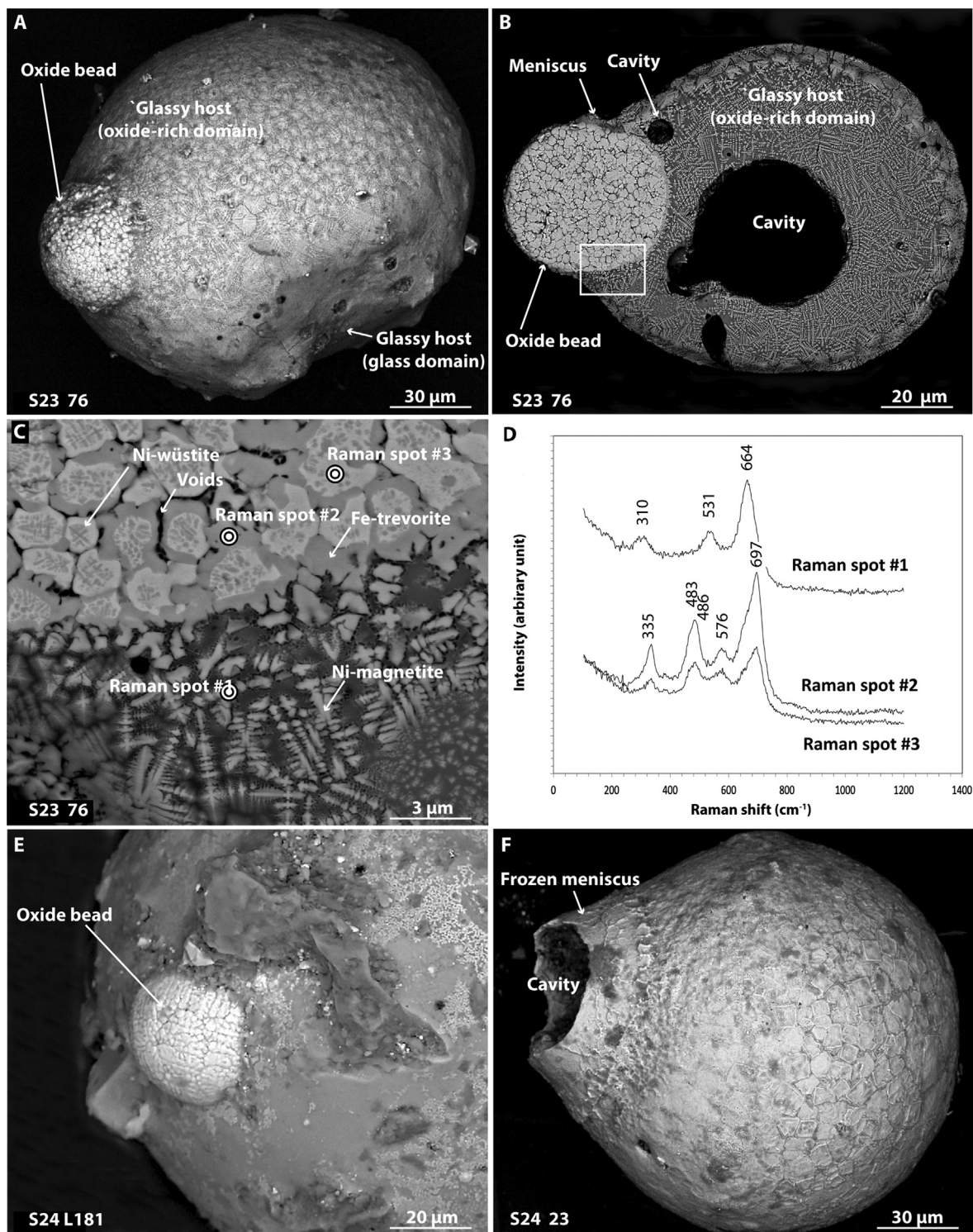


Fig. 9. Compound spherules S23 76 (A to C, BEI; D, Raman spectra), S24 L181 (E: BEI) and S24 23 (F: BEI). A) Whole S23 76 spherule showing an oxide bead (arrowed) embedded in a glassy spherule. Note the gradual change of mineral composition of the glassy host spherule showing a progressive increase of dendritic Fe-Ni oxides moving towards the oxide bead. B) A section through the Fe-Ni oxide-rich domain of the host spherule and the oxide bead (arrowed). The former has vitrophyric texture with microscopic Ni-bearing magnetite dendrites set in a Fe-rich glass. The latter has microscopic globular texture and consists of Ni-wüstite grains with exsolved cores rimmed by Fe-trevorite. A relatively large, rounded cavity occurs near the center of the host glassy spherule. C) Raman spectra location map featuring a detail of the contact between the glassy host spherule and oxide bead. Note the similarity between the bead and spherule S24 24, and the host spherule and spherule S23 L5. D) Raman spectra of exsolved Ni-wüstite cores (#3) and Fe-trevorite in bead (#2) and Ni-bearing magnetite in the host spherule (#1). E) A portion of the external surface of spherule S24 L181 showing a protruding Fe-Ni oxide bead. F) The oxide-rich spherule S24 23 showing a large spherical cavity at one tip and frozen meniscus.

The Fe-Ni oxides in the oxide spherules are Ni-wüstite, trevorite and Ni-magnetite. The study of their mineralogical evolution in terms of crystallization temperatures, compositions and textures

can be approached referring to the Fe-Ni-O system, revised by Raghavan (2010), using the equilibrium Fe-Ni-O pseudo-binary section in air along the Fe_2O_3 -NiO join shown in Fig. 11. Although

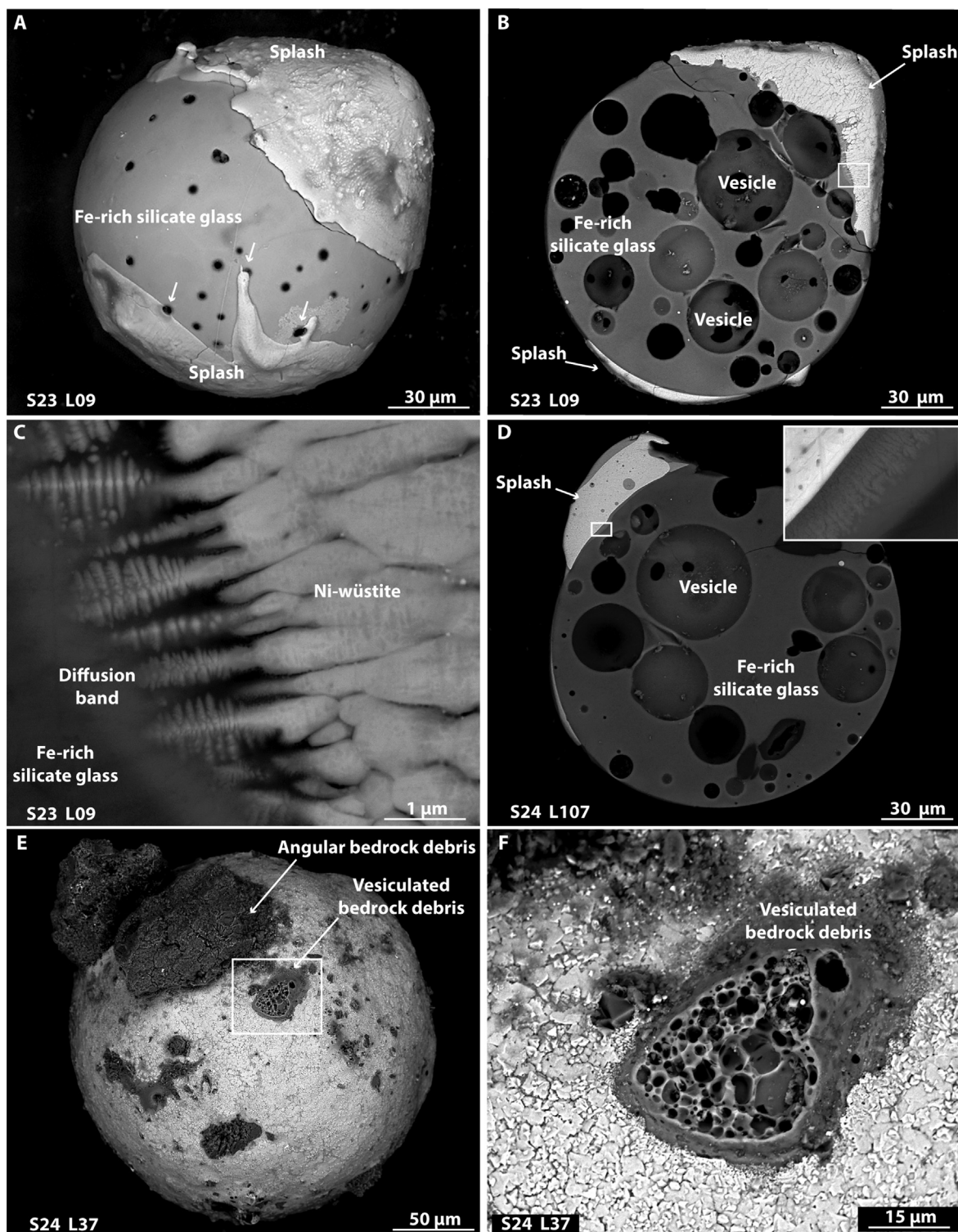


Fig. 10. Melt splashes and target debris stuck on external surface (A to F: BEI). A) Oxide splashes on Fe-rich silicate glass spherule S23 L09. Cross-cut relations between streamlets of the oxide splash and vesicles in the glass of the host spherule are arrowed. B) A section of the same spherule through the two oxide splashes consisting mainly of Ni-wüstite and the host sphere consisting of highly vesiculated Fe-rich glass. Note the contrast between the sharp contact of one splash which follows the spherical surface of the host spherule at the bottom of the image (cold contact), and the embayed contact of the other splash which disrupts the sphericity of the host spherule on the other side (hot contact). C) A close-up view of the hot contact (see white rectangle in B for location). Microscopic, elongated Ni-wüstite dendrites extend into the Fe-rich silicate glass of the host spherule within a diffusion band (brighter Z-contrast). D) Section of the similar spherule S24 L107; the splash, however, consists of a cap of Fe-Ni metal alloy topped by an oxidized layer. Inset: a detail of the hot metal splash-glass host spherule contact. E) Angular bedrock fragments and silicate-glass bedrock debris on the external surface of spherule S24 L37. The white rectangle outlines the feature shown in F). F) A close-up view of the silicate-glass bedrock debris partially entrained in spherule S24 L37 showing high vesiculation. Note the corona (diffusion band) indicative of hot accretion.

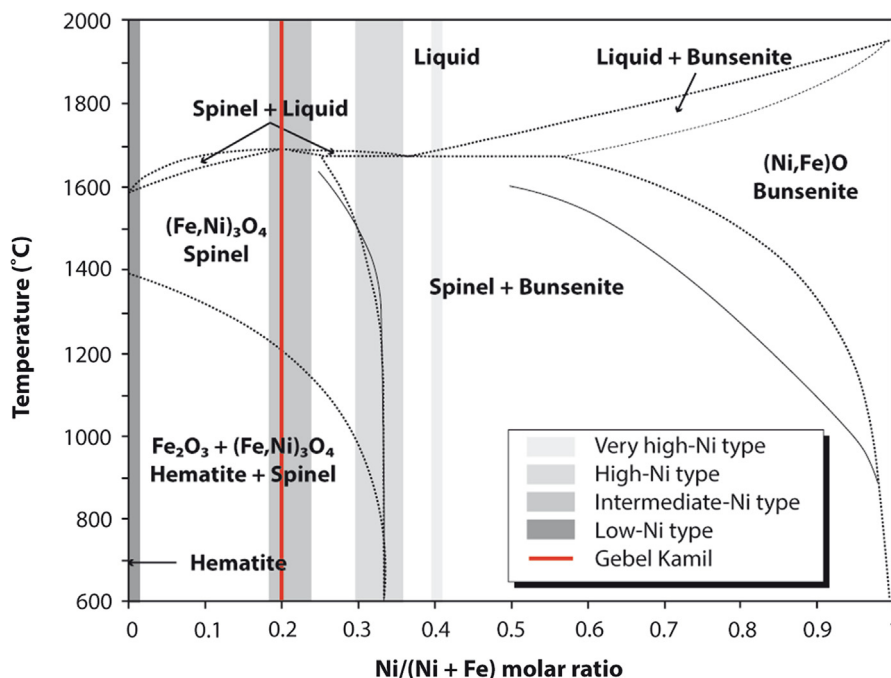


Fig. 11. Equilibrium Fe-Ni-O pseudo-binary section in air along the Fe_2O_3 -NiO join (modified after Raghavan, 2010). The Ni/(Ni + Fe) molar ratios of the Fe-Ni oxide spherule bulk composition (EDS analyses; Table 3) of the very high-Ni, high-Ni, intermediate-Ni and low-Ni compositional types are shown. The Ni/(Ni + Fe) molar ratio of Gebel Kamil (red line) is from D'Orazio et al., 2011). Dotted curves are calculated; solid curves are experimentally derived.

discrepancies between thermodynamically calculated and experimental curves along with evidence of disequilibrium crystallization in the studied oxide spherules (i.e., skeletal habits and microscopic grain size) requires caution, we observe a substantial consistency with the observed crystallization sequences inferred from our petrographic analyses.

For a Ni/(Ni + Fe) molar ratio of ~ 0.40 , as measured in the very high-Ni spherule S24 24 and in the bead of the S23 76 compound spherule, the equilibrium phase diagram predicts crystallization of bunsenite first, immediately followed by the eutectic crystallization of bunsenite (or better, a phase of the bunsenite-Ni-wüstite series; see nomenclature adopted in this paper discussed in Chapter 2) plus spinel at around 1660 °C, and their subsequent exsolution under subsolidus conditions due to an immiscibility gap. In the oxide spherules of the very high-Ni compositional type, we observe that Ni-wüstite with Ni/(Ni + Fe) molar ratio of ~ 0.50 is the dominant phase, forms globular grains with exsolved cores and homogenous rims, and is surrounded by subhedral intergranular trevorite or Fe-trevorite and voids. Here the crystallization sequence is Ni-wüstite cores followed by Ni-wüstite rims plus intergranular trevorite, followed by the subsolidus formation of fine trevorite exsolutions in the Ni-wüstite cores. The lack of exsolutions in the adjacent Ni-wüstite rims and trevorite, at least at the SEM scale, may be due to the combination of direct Fe-Ni interdiffusion at grain boundaries and of the limited compositional change predicted for the subsolidus evolution of Ni-spinel. Unfortunately, we do not have the compositions of the exsolved phases in the Ni-wüstite cores due to their small size (nanoscale) relative to the electron beam of the EPMA (microscopic). However, the bulk core has a Ni/(Ni + Fe) molar ratio of ~ 0.50 and the surrounding trevorite or Fe-trevorite of ~ 0.19 – 0.30 , suggesting closure temperatures of the Fe-Ni diffusion no lower than ~ 1550 °C, consistent with the quench textures of the spherules.

For lower Ni/(Ni + Fe) molar ratios of ~ 0.33 and ~ 0.20 , as measured in the bulk Fe-Ni spherules of the high-Ni and intermediate-Ni compositional types, respectively, the equilibrium

phase diagram predicts the opposite sequence of crystallization which is roughly what we observe in the corresponding spherule types (Figs. 3 and 4). These are dominated by finely exsolved trevorite or Fe-trevorite with smaller intergranular or interstitial Ni-wüstite grains, respectively (Table 1).

The Fe-Ni oxide spherules of the intermediate-Ni compositional type with vitrophyric textures (Fig. 5) and those of the low-Ni compositional type (Fig. 6) have bulk compositions that do not strictly fit into the Fe-Ni-O system, due to the occurrence of Fe-rich silicate matrix up to ~ 15 vol%. Spherules of the intermediate-Ni compositional type however mainly consist of equant cruciform dendrites of Fe-trevorite with homogenous composition plus smaller amounts of intergranular or interstitial Ni-wüstite grains set in a Fe-rich silicate matrix. Overall, their crystallization history is similar to that of the other Fe-Ni oxide spherules of the intermediate-Ni compositional type, except for the lack of exsolutions probably due to quenching at crystallization temperatures of ~ 1660 °C, i.e. above the immiscibility gap. Spherules of the low-Ni compositional type mainly consist of equant cruciform dendrites of Ni-magnetite with homogenous composition set in a Fe-rich silicate matrix (see below). Similarly, the lack of exsolutions in Ni-magnetite would indicate quenching from crystallization temperatures of ~ 1600 °C.

The matrix of the Fe-Ni oxide spherules belonging to the low-Ni compositional type consists of coalescent submicroscopic domains characterized by contrasting Z with vermicular to mottled textures as revealed by BEI (Fig. 6E). The size of the individual vermicular domains is beyond the analytical capability of a microprobe. However, WDS analyses (Table 4), likely representing the bulk composition of the matrix, indicate high concentration of Fe (49.9–61.2 wt%) and Si (4.44–11.1 wt%), with minor Ni (0.5–1.9), Al (0.06–1.4), P (0.44–2.28), and EDS analyses suggest higher concentrations of Fe and Si in the domain with high and low Z-contrast, respectively. As mentioned above, these microstructures resemble emulsions of silica and Fe-rich glasses with interconnected morphologies, resulting from phase separation of immiscible silicate liquids. This kind of microstructures have been previously

described in impact melts from other impact structures, including in the dark glass from Kamil (Fazio et al., 2016; Hamann et al., 2018). Such emulsion textures occur also locally within the Fe-rich silicate matrix of the Fe-Ni oxide spherules with vitrophyric textures of the intermediate-Ni compositional type (Fig. 5D and 5E).

Most of the studied oxide spherules have one large hollow cavity towards their cores. They often have irregular outlines defined by the forms of the dendritic crystals of the host oxides (e.g., Figs. 2, 3 and 4). In other instances, they have smooth, nearly perfect spherical shapes (e.g., Fig. 6C). They are likely the result of the inward crystallization of the oxide dendritic crystals, combined with the presence of a gas phase when spherical. The inward crystallization is consistent with the inward increase of interstitial phases observed in some spherules (Fig. 4D). The microscopic intergranular voids observed in virtually all the oxide spherules (e.g., Figs. 3, 4 and 5) have similar morphologies and may be contraction voids due to the change in specific volume during solidification, possibly supported by a gas phase.

The metal sphere S24 L165 (Fig. 8) is dominated (97 vol%) by globules of Fe-Ni alloy surrounded by thin films of P-bearing sulfide matrix material (Table 3), with a very thin shell of Fe-Ni oxides in a silica-rich matrix. The overall texture is the result of metal-sulfide immiscibility. The metal alloy has homogeneous taenite composition (Ni = 22.1 wt%; Table 4). The lack of accurate composition of the sulfide matrix prevents precise estimates of the solidification temperatures, although the solidus of the Fe-Ni-S system constrains crystallization temperatures above 800 °C (Kellerud, 1962). The metallic splash of spherule S24 L107 has homogenous taenite composition indicating quenching from over 1500 °C (Yang et al., 1996).

The oxide-rich spherule S23 L5 shows evidence of oxidation decreasing towards the spherule center, likely in air during ejection (see below). This is a mineralogical zoning with Ni-bearing wüstite dominating its core and Ni-bearing magnetite its periphery, with a nearly continuous rim of Ni-bearing magnetite at its surface. Likewise, the oxide-rich shell of the S24 L165 metal sphere and the oxide layer enveloping the L24 107 metal splash are indicative of partial oxidation from the outside moving inward. In S24 L165 preservation from complete oxidation could have been facilitated by the occurrence of sulfur in the system, which could act as a reducing agent. The oxide-rich covers make this type of spherules indistinguishable from the other oxide spherules based on external surface examination only.

4.2. Formation by impact melting and separation during ejection

From the Fe, Co, Ni diagrams in Fig. 12 A,B we conclude that all the oxides and metal alloys composing the Fe-Ni oxide and metal spherules from Kamil belong to a single compositional population of quenched droplets of high temperature oxide or metal liquids, in spite of their large variety of textures and compositions. Iron varies from ~33 to ~71 wt% and is negatively correlated with Ni, which ranges from ~1 to 40 wt% Ni. The linear fit gives rise to a negative slope of -0.9 and a coefficient of determination R^2 of 0.97. Cobalt varies from ~0.02 to 1.41 wt% and, despite some scatter, is positively correlated with Ni. The linear fit gives rise to a positive slope of 25.1 with an R^2 of 0.831 and intercept of ~0.18, next to the origin. The Ni/Co average value is 25.1 ± 7.6 (Table 4). The metal sphere S24 L165 (Fig. 8) and splash S25 L107 (Fig. 10) plot on the same trend in the Ni vs Co space.

But how about the petrogenesis of the Fe-Ni oxide and metal spherules? This question was posed by Folco et al. (2015) who first reported on this kind of metallic spherules in their inventory of microscopic impactor debris dispersed in the soil around Kamil. Based on a preliminary mineralogical and geochemical analysis,

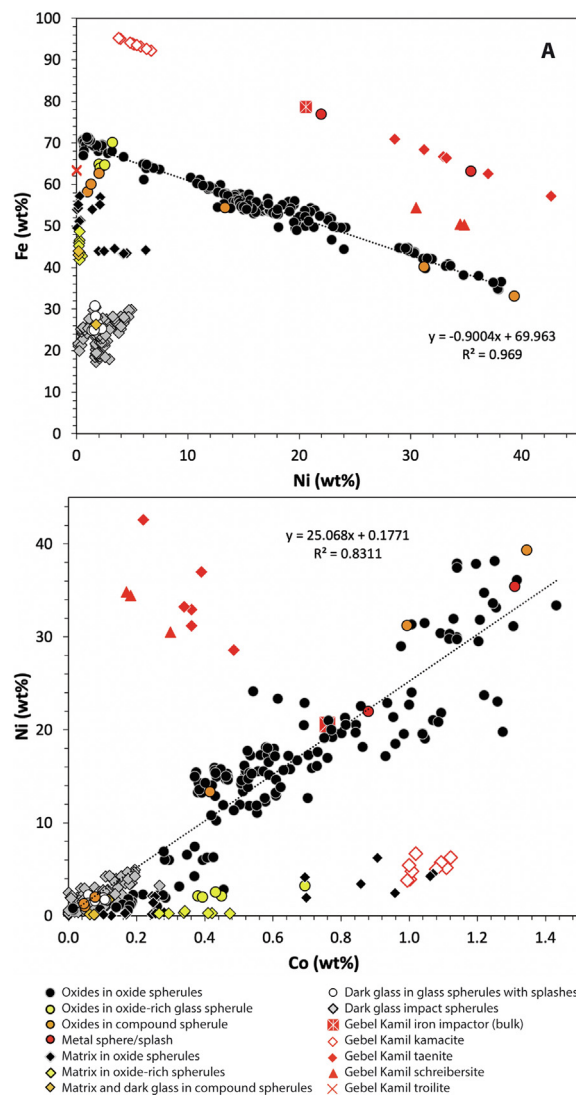


Fig. 12. Binary Fe-Co-Ni (wt%) compositional diagrams for the mineral components of the Fe-Ni oxide and metal spherules from Kamil (see Table SM1 for data set). Data for Gebel Kamil (bulk rock and mineral inclusions) and Kamil impact glass spherules from the literature (D'Orazio et al., 2011; Fazio et al., 2016) are shown for comparison. A) Iron versus Ni. B) Nickel versus Co.

they suggested an origin by impact melting most likely. However, they also pointed out a close similarity with i) I-type cosmic spherules (Genge et al., 2008, 2017; Folco and Cordier, 2015), produced by the oxidation and melting of metal micrometeoroids during atmospheric entry; and ii) with the Fe-Ni oxide spherules found at the Sikhote Alin (Russia) crater field and interpreted as ablation spherules (Badyukov and Rajtala 2012), i.e. formed late during the fall of the Sikhote Alin meteorite through the melting of debris produced during its disintegration. The larger data set gathered in this work allows us to support an origin by impact melting, due to the hypervelocity impact of the iron projectile Gebel Kamil against a SiO₂-rich sedimentary target. The former consists of a Ni-rich (20.6 wt% Ni) ataxite; the latter of quartz-arenites and wackes with siltstone levels (Table 4) plus minor kaolinite. This conclusion is based on the following arguments.

4.2.1. An impact melting context

Silica and alumina are the main components of the sedimentary target rocks at Kamil and are not contained in the Gebel Kamil iron meteorite impactor (Table 4). The occurrence of Si and Al in the

bulk of all Fe-Ni oxide spherules, their constituent oxides and matrix, from trace to significant amounts, requires target-projectile interaction. The mineral chemistry of the Fe-Ni oxide spherules fits into the target – projectile mixing trend defined by silicate impact melts from Kamil described in the literature in the Si + Al vs Fe + Ni space (Fig. 13). This geochemical evidence rules out an origin as ablation spheres which forms during the ablative flight of meteorites through the atmosphere.

A geochemical affinity between the Fe-Ni oxide spherules and the Gebel Kamil iron impactor is provided by their Fe, Co, Ni ratios. The slope value of the linear fit of the Fe-Ni oxide compositions in the Ni vs Co space (25.1) and the median Ni/Co ratio (25.1 ± 7.6) are consistent with the Ni/Co ratio in the Gebel Kamil impactor, namely 27.1 (Fig. 12 and Table 4). Likewise, the average Ni/(Ni + Fe) molar ratio of 0.21 ± 0.13 of the Fe-Ni oxide is indistinguishable with the value of the bulk impactor of 0.20 (Table 4).

The contrasting spherule distribution around the crater is also consistent with an impact origin. The high abundance of Fe-Ni metallic spherules due SE of the crater and their lack due NW of the crater fits with the NW-SE trajectory of the impactor and downrange ejecta distribution defined by D'Orazio et al. (2011) and Urbini et al. (2012).

Virtually all the studied spherules are speckled with quartzose \backslashclay rock fragments or silica glass patches welded to their external surfaces (e.g., Figs. 4B and 5A,B; Table 1). This is bedrock debris accreted in the impact plume during ejection. A similar mechanism can account for the Fe-Ni oxide splashes on the impact glass spherule S23 L9 (Fig. 10B,C). The latter is similar to the individual oxide spherule S24 24, a type of spherule that must have been common in the impact plume.

4.2.2. Residues of immiscible projectile melt droplets

The compound spherule S23 76 (Fig. 9A-C) provides evidence for the formation of the Fe-Ni oxide and metal spherules as residues of immiscible projectile melt droplets originally dispersed in the Kamil dark glass. In this spherule we have the association of a Fe-Ni oxide bead, tens of μm in diameter, partially embedded in a larger glassy spherule which shows a progressive enrichment of Fe-Ni oxides towards the bead. Remarkably, we observe a close compositional and textural similarity between this bead and the

individual spherule S24 24 (Fig. 2), and between the oxide-rich domain of the host spherule and the individual spherule S23 L5 (Fig. 7). Likewise, the glass domain of the host spherule is indistinguishable from the Kamil “dark glass”, which is one of the two end-member compositional impact glasses composing impact melt bombs, lapilli and impact glass spherules dispersed around the crater (Table 4), described by Fazio et al. (2014, 2016) and Folco et al. (2015). This implies that the precursor liquids of Fe-Ni oxide spherules originate within the Kamil dark glass, consistently with the detection of Si (and, to a lesser extent, Al) in all Fe-Ni oxide spherules and/or their constituent minerals.

Scattered, tiny, Fe-Ni metal blebs, sometimes up to 200 μm in diameter, have been observed in the Kamil dark glass of the impact melt bombs, lapilli and impact glass spherules (Fazio et al., 2014, 2016; Folco et al., 2015; Hamann et al., 2018). They consist of Fe-Ni metal alloys with featureless or, occasionally, globular textures with minor P-bearing sulfide matrix. Because of their enrichment in Ni (and Co) relative to Gebel Kamil (with Ni concentrations up to ~94 wt%) and Ni/Co ratios close to that of Gebel Kamil they were interpreted as fractionated droplets of the metallic liquid of the projectile under varying oxidizing conditions. For the similar petrographic setting (i.e., the Kamil dark glass) and elemental ratios, we thus suggest that the precursor liquids of the Fe-Ni oxide spherules from Kamil are the product of the oxidation of metal droplets like those frequently observed as blebs in the Kamil dark glass (Fazio et al., 2016).

The chemical fractionation under oxidizing condition is exemplified by what we can observe in spherule S23 76 (Fig. 9A-C). Here the Ni/(Ni + Fe) molar ratio drops from the high value of 0.44 in the bulk oxide bead to ~0 in the adjacent oxide-rich domain of the host glass spherules (Table 3), to then slightly increases to 0.06 in its oxide free dark glass region (Table 4). Thus, the bead is enriched in Ni relative to Fe compared to Gebel Kamil [Ni/(Ni + Fe) molar ratio of 0.20; Table 4], whereas the host glass is progressively enriched in Fe moving away from the bead. This chemical fractionation can be explained by considering that iron is preferentially oxidized relative to Ni and the partition coefficient between a metallic and a silicate melt of Ni is higher than that of Fe (e.g., Righter et al., 1997). For these reasons, Fe-Ni metal liquids interacting with a silicate liquid under oxidizing conditions can produce Fe-Ni oxide dominated liquids adjacent to Fe-dominated silicate liquids (e.g., Hamann et al., 2018). These are the precursor liquids of the Fe-Ni oxide bead and the adjacent oxide-rich domain of the glass host spherule in S23 76. By extension, we conclude that this oxidation-driven fractionation process can locally produce liquids of the whole compositional range of the Fe-Ni oxide and oxide-rich glass spherules studied in this work, namely with bulk Ni/(Ni + Fe) molar ratios higher and lower than that of the Gebel Kamil precursor, as well as the metal spherule and splash with bulk Ni/(Ni + Fe) molar ratios higher than Gebel Kamil (Tables 3 and 4). The extent of the compositional variations is a function of the extent of the chemical interaction with surrounding melt in terms of time and degree of oxidation.

In the fractionation process described above, Co and Ni behave similarly, as shown by their positive correlation observed in the Fe-Ni oxides within the Fe-Ni oxide spherules (Fig. 12). As mentioned above, despite some scatter, the distribution of the compositions of the entire population of Fe-Ni oxides studied in this work defines the Ni/Co ratio of the Gebel Kamil precursor material (~27), suggesting limited Ni versus Co fractionation during the impact melting process. This also suggests an overall homogenization of the precursor liquid upon impact melting, considering that the Gebel Kamil ataxite contains ~2% by volume of scattered mm-sized mineral inclusions consisting of associations of daubréelite, schreibersite and troilite in swathing kamacite plus taenite (D'Orazio et al., 2011). In this context, the occasional occurrence

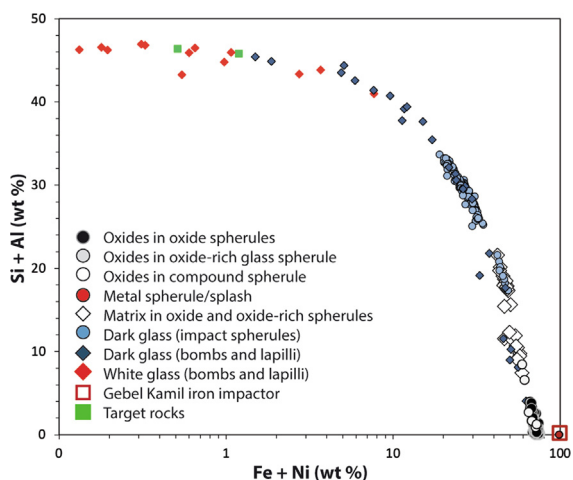


Fig. 13. Silicon + Al vs Fe + Ni (wt%) diagram for the mineral components of the Fe-Ni metal spherules studied in this work, along with data for target rocks, Gebel Kamil iron meteorite impactor and impact melt bombs and lapilli of the dark and white compositional types from the literature (Fazio et al., 2014, 2016). The data set defines a mixing curve between the target and the impactor, consisting of Cretaceous sandstones and minor wackes, and an ungrouped Ni-rich ataxite, respectively (see Table 4 for element concentrations).

of P ± Cu bearing metal nuggets in some oxide spherules (e.g., Figs. 3, 4, and 5) and of minor concentrations of Cr in spherule S23 77 (Table 4) can be explained by the occurrence of daubrélite, schreibersite and native Cu (D'Orazio et al., 2011) in the Gebel Kamil precursor. Also, the Ni/Co ratios (~5) observed in the Ni-bearing wüstite and Ni-bearing magnetite in the oxide-rich glass spherule S23 L5 are similar to Gebel Kamil kamacite (Table 4; Fig. 12B), hinting for a kamacite dominated Gebel Kamil precursor material.

4.2.3. Separation into individual spherules

The comparison of spherules S24 L181 and S23 76 provides evidence for the physical separation of the Fe-Ni oxide and metal spherules from the dark glass they originated in. The occurrence of compound spherules with ovoid shapes and oxide beads protruding through their external surface along their axis of elongation as well as other spherules with ovoid shapes and one large hemispherical cavity at one tip with frozen meniscus (Fig. 9A,E,F) suggests bead stripping and separation of the two immiscible liquid spherules whilst still hot and plastic within the impact plume. This mechanism is expected to occur during ejection and fragmentation of the impact melts from the transient crater cavity. Travel through Earth's oxygen-rich atmosphere facilitated further and rapid oxidation. Separation is due to the application of strong accelerations associated to supersonic ejection velocities (of several km/s, on the basis of estimates of the contact velocity for the Kamil impact; Fazio et al. 2016) to spherules with high-density contrast and/or spinning. A similar separation process is well documented in I-type cosmic spherules, although in the context of strong deceleration from cosmic velocities in the upper atmosphere (e.g., Brownlee and Bates, 1983; Genge et al., 2017).

4.2.4. Late accretion

The external surfaces of almost all the studied spherules are speckled with welded bedrock debris, including sandstone or kaolinite as angular fragments and silica-rich glass or lechatelierite patches (Figs. 4, 5, 7, 8, 10). Some other spherules are coated with splashes of other droplets. This is evidence of accretion of cold or hot debris during the ballistic flight in a dense and turbulent impact plume. Diffusion bands at the contact between host spherules and accreted debris, as observed in some specimens (Fig. 10C, D,F), are indicative of some geochemical mixing at high temperatures. Although these diffusion bands are of limited extension (a few µm in thickness), they show that impact spherules may undergo further geochemical evolution, although limited to their external surface, due to late accretion during their flight.

The debris accreted onto the studied spherules includes sandstone, wackes and kaolinite fragments. This is in fact an inventory of the lithologies of the target rocks at Kamil. Thus, the petrographic study of the external surfaces of impact spherules can provide clues about the nature of the target rocks; this could be particularly useful in the case of missing parent craters, as is for the Australasian tektite/microtektite forming impact event (Glass et al., 2004).

4.2.5. The model

We can envision a formation scenario for the Fe-Ni oxide and metal spherules within the framework of the impact melting model proposed by Fazio et al. (2016) and Hamann et al. (2018) for Kamil (Fig. 14). Impact melting is characterized by strong disequilibrium due to the very short duration, on the scale of a few seconds, of small impact events like Kamil. During the contact and compression stage (Fig. 14A), peak shock pressures in excess of 30 GPa are attained at the contact point between projectile and target. Kinetic energy of the projectile is converted into heat while shock waves propagate both into the projectile and in the target.

At the transition from the contact and compression stage and before the excavation stage, an intermediate stage named “end of contact and compression stage” occurs, which is fundamental for the formation of impact melts and the chemical-physical interactions between projectile and target (see Ebert et al., 2014).

At this stage, a rarefaction wave, produced when the shock wave is reflected at the rear surface of the projectile, moves downward through the projectile and then through the target. The passage of this rarefaction wave leads to decompression, heating and melting of the target and the projectile under oxidizing conditions (Fig. 14B), and then to the ejection of meteorite shrapnel, impact melt masses and target fragments during the subsequent excavation stage. Both the projectile and target rocks melt along the interface. Here, before ejection, the projectile melt is injected into the target melt. The latter consists of two silicate liquids reflecting the heterogeneity of the source rock: a silica melt and an Al-rich melt. Due to the high degree of polymerization, the SiO₂ melt does not geochemically interact with the projectile melt giving rise to silica glass, the Kamil white glass. In turn, the Al₂O₃-rich silicate melt does interact (mixing, fractionation) with projectile melts, due to its lower degree of polymerization; this gives rise to an Fe-Al-rich silicate liquid, the Kamil dark glass, with dispersed Ni-Fe metallic blebs, immiscible residues of the projectile liquid. At this point excavation starts, the melt is ejected. Hypervelocity ejection produces fragmentation of the melt material producing impact melt bombs, lapilli and a spray of molten spherules undergoing further and variable oxidation (Fig. 14C). Meanwhile the Ni-Fe metal blebs interact with the host dark glass and Fe is fractionated from the blebs into the surrounding glass (Fig. 14D). A passive enrichment of Ni (plus Co) occurs in the metallic blebs to form the Fe-Ni oxide spherule precursor liquid. In the dark glass spherules, differential acceleration due to density contrast separates such liquid droplets from the host. The Fe-Ni oxide spherules are liberated within the impact, leaving behind an oxide-rich glass spherule. These spherules collide with other spherules or accrete bedrock debris entrained in the plume while still hot and plastic, and later quench in air (consistent with the observed inward crystallization; see above) before landing on the ground.

Conceivably, one could argue that the Fe-Ni oxide spherules, or at least some of them simply represent physically separated projectile melt droplets that never experienced extensive interaction with the target melts. However, we have no evidence in support of this argument yet. All the Fe-Ni spherule types (and their constituent phases) studied in this work contain Si and Al from the target and, therefore, they necessarily underwent some physical-chemical interaction with target melts. Also, the Fe-Ni metallic spherule S24 L165 is enveloped by a shell of oxide-rich silicate glass. Finally, the Fe-Ni metallic splash S24 L107 has indeed a bulk Ni/(Ni + Fe) molar ratio similar to the Gebel Kamil taenite inclusions (0.35 and 0.33, respectively; Table 4) hinting for a direct derivation from a taenite-rich liquid; yet, the Ni/Co ratio does not match Gebel Kamil taenite (27 and 104, respectively; Table 4), but does match that of the bulk Gebel Kamil of 27. The lack of pure projectile Fe-Ni spherules in the studied set was unexpected and calls for further systematic studies on a even larger population of spherules. Nonetheless, the present statistics suggests that the dominant mechanism for the formation of individual Fe-Ni oxide spherules is the one proposed here which requires target-projectile melts interactions.

Although Fe-Ni metallic droplets dispersed in projectile-rich silicate impact melt rocks, have been described from several impact craters produced by iron impactors [e.g., Wabar (Saudi Arabia), Brett, 1967; Gibbons et al., 1976; Hamann et al., 2013; Monturaqui (Chile), Bunch and Cassidy, 1972; Gibbons et al., 1976; Henbury (Australia), Gibbons et al., 1976; Barringer Crater (Arizona, USA) Hörz et al., 2002; Kearsley et al., 2004], individual Fe-Ni metal-

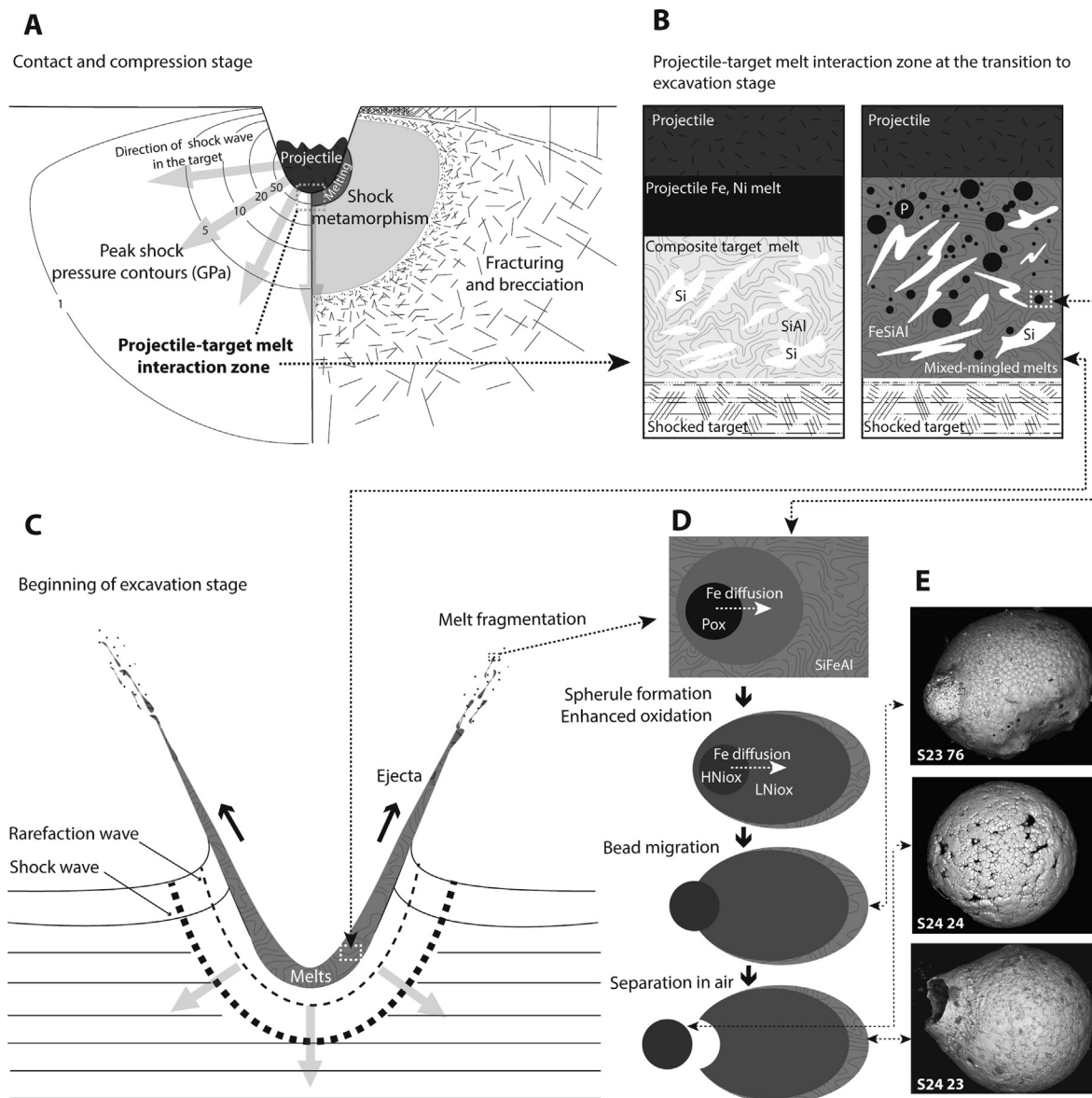


Fig. 14. The formation model of Fe-Ni oxide impact spherules at Kamil crater (45 m in diameter). A) Schematic cross section depicting the contact and compression stage in the formation of a simple crater (modified after Melosh, 1989); isobars of peak shock pressures (left) and corresponding effects in the target rocks (right) are shown. The impactor-target melt interaction zone described below is outlined (dashed grey rectangle). B) The projectile-target melt interaction zone at the end of the contact and compression stage (modified after Fazio et al., 2016). A projectile and target liquids (namely, an Al-rich silicate and a virtually pure silica immiscible liquids) are formed under oxidizing conditions (left panel) and chemically and physically interact at the contact zone (right panel). The geochemical interaction between the projectile melt and target Al-rich silicate melt under oxidizing conditions generated a mixed melt which eventually gave rise to the Fe-Al-rich silicate dark glass. Interaction is not complete (disequilibrium) and microscopic blebs of projectile melt residues remain afloat, undergoing variable oxidation and Fe-Ni fractionation. The other immiscible target silica melt did not geochemically interact with the projectile and eventually gave rise to the white glass. C) Schematic cross section depicting the beginning of the excavation stage (modified after Osinski and Pierazzo, 2013). The ejecta curtain contains impact melts that fragment upon high velocity ballistic ejection giving rise to bombs, lapilli and spherules. E) Spherules containing high-density Fe-Ni metallic and oxide beads physically separate to form individual Fe-Ni oxide spherules and oxide-rich spherules by stripping during hypervelocity ballistic ejection. F) This sequence of events is exemplified by the compound spherule S23 76 (Fig. 9A), the very high-Ni type Fe-Ni oxide spherule S24 24 (Fig. 2A) and the low-Ni type oxide-rich spherule S24 23 with a large spherical cavity at one tip (Fig. 9F). Abbreviations: Si = silica melt or the Kamil white glass; SiAl = Al-rich silicate melt; FeSiAl = Fe-Al-rich silicate melt or the Kamil dark glass; P = projectile melt; Pox = oxidized projectile melt; HNiox = high-Ni, Fe-Ni oxide liquid; LNiox = low-Ni, Fe-Ni oxide liquid.

oxide spherules have been reported previously only from Barringer Crater (e.g., Kelly et al., 1974; Mittlefehldt et al., 2005) and possibly from Whitecourt, Alberta, Canada (Kofman et al., 2010). Formation models for these individual metallic impact spherules are only discussed for those recovered at Barringer. Based on a geochemical investigation, Kelly et al. (1974) proposed that metallic spherules from the Barringer projectile formed liquid droplets recording a Fe, Ni, Co (plus Cu) fractionation in terms of mode and extents due to varying degrees of oxidation similar with what is observed at Kamil in this work. However, they suggested that oxidation was

caused by oxygen uptake in air during their high velocity flight of projectile melt droplets without mentioning the possibility of an origin and first oxidation as immiscible projectile liquids within an impact melt consisting of a mixture of target and projectile liquids, as proposed here.

We suggest that the model for the formation of individual Fe-Ni oxide spherules proposed here applies to all impact events produced by iron (or stony-iron) impactors, including the above and perhaps many others, like Kaalijarv (Estonia), Campo del Cielo (Argentina), Morasko (Poland), Sobolev (Russia), Odessa (USA),

Boxhole and Wolfe Creek (Australia), Macha, Auelloul (Mauritania), and that such spherules are common impact products. Also, considering their higher resistance to weathering relative to other microscopic impact melting products like, for instance, the silicate glass spherules, they should be good markers of impact craters produced by iron impactors in the sedimentary record of the geological past.

4.3. Discrimination from other similar spherules in the geologic record

The pristine petrography and geochemistry of the Fe-Ni spherules found at Kamil offers a unique opportunity to discuss diagnostic features for their discrimination from similar spherules in the geologic record. Previous studies of Fe-Ni spherules from Barringer Crater focused on their distribution around the crater and geochemistry (Nininger, 1956; Rinehart, 1957; Blau et al., 1973; Kelly et al., 1974), with little or no petrographic information. This is also the case for the Fe-Ni-rich spherules mentioned in the discovery report of the Whitecourt crater (Kofman et al., 2010), while our previous report on the Kamil spherules (Folco et al., 2015) provided only a limited view of their petrographic and geochemical diversity.

The Fe-Ni oxide spherules from Kamil share a number of petrographic features with similar spherules found at the Earth's surface and extracted from terrestrial sediments. These formed by similar petrologic processes, namely melting of meteoritic iron precursors under oxidizing conditions, but in different natural contexts. As mentioned in Chapter 4.2, they include I-type cosmic spherules (Genge et al., 2008, 2017; Folco and Cordier, 2015) and iron meteorite ablation spherules (Badyukov and Rajtala, 2012). Their discrimination through diagnostic features is thus fundamental to place them into the correct geologic context, particularly in the view of the growing interest in the search for fossil micrometeorites and impact spherule layers in the sedimentary record, possibly linked to periods of enhanced flux of extraterrestrial dust to Earth and associated with catastrophic break-up events in the Asteroid Belt, or to major asteroidal or cometary impacts through Earth's geologic history (e.g., Schmitz, 2013; Suttle and Genge, 2017; Tomkins et al., 2016).

In Chapter 2.4, we demonstrated that target contamination, namely, a target geochemical signature and/or accreted target material on the external surfaces, is a strong discriminating factor. Target contamination is obviously inconsistent with formation high in the Earth's atmosphere (the thermo-mesosphere) as in the case of I-type cosmic spherules (e.g., Love and Brownlee, 1991; Genge et al., 2017), or lower down to the high troposphere as for the ablation spherules (Badyukov and Rajtala, 2012). However, distinction based on the mere petrographic comparison of observations of sectioned particles is not straightforward as the target geochemical signature in the composing minerals may not be obvious, especially in the case of little or no silicate matrix.

I-type cosmic spherules are produced by the oxidation and melting of metal micrometeoroids derived from chondritic precursors by collisional liberation during atmospheric entry. They are classified into two mineralogic groups based on their extent of oxidation (Genge et al., 2017): i) metal bead-bearing spherules (MET) retain some of their pre-atmospheric unoxidized metal – this appears as an off-center Fe,Ni metal bead (10–95 wt% Ni) held within an oxide shell composed of microscopic interlocking dendrites of Ni-poor wüstite ($\text{Ni} = 0.3 \pm 6.5$ wt%; range 0.1–6.5 wt%) with minor magnetite; ii) metal bead-free oxide spherules (OX) are completely oxidized and lack surviving metal; instead, they are dominated by microscopic interlocking dendrites Ni-rich wüstite ($\text{Ni} = 3.0 \pm 3.1$ wt%; range 0.1–11.3 wt%) and magnetite ($\text{Ni} = 3.6 \pm 2.1$ wt%, range: 0.3–9.2 wt%). The latter are petrographically similar to the Kamil Fe-Ni oxide spherules which are devoid of silicate matrix, like those belonging to the very high-Ni, high-Ni

and intermediate-Ni compositional types (compare for instance spherules featured in Fig. 2A of this work with Fig. 3d,e,f in Folco and Cordier, 2015), despite a stark contrast in Ni content ($\text{Ni} \sim 3 \pm 3$ vs > 10 wt% in I-type cosmic spherules and Fe-Ni oxide spherules from Kamil, respectively; Table 4). Yet this compositional difference is simply a reflection of compositionally different precursors. Note that Gebel Kamil – the Kamil projectile – is a Ni-rich and anomalous ataxite (D'Orazio et al., 2011).

Fe-Ni oxide spherules were reported from the Sikhote Alin (Russia) crater field and interpreted as ablation spherules produced by the fall of the Sikhote Alin iron meteorite, through the melting of debris during its disintegration (Badyukov and Rajtala, 2012). These spherules have fine-grained quenched textures and are dominated by Ni-bearing magnetite (3–6 wt% Ni) dendrites, occasionally with interstitial P and Fe-rich silicate matrix with an overall composition close to fayalite with minor Al, Na and K. In some spherules magnetite is associated with minor wüstite. Although either somewhat enriched or depleted in Ni, the oxides in most of these spherules have Fe/Ni and Ni/Co element ratios close to those of the bulk composition of the Sikhote Alin meteorite (Fe/Ni ~ 15.7 ; Ni/Co ~ 12.1), documenting their parentage with the iron projectile. The presence of interstitial silicate material was attributed to the possible occurrence of silicate inclusions in the parent meteorite.

The similarity of some of the ablation spherules from Sikhote Alin, particularly those with interstitial silicate matrix, is overwhelming. Compare, for instance, spherules S25 L11, and S25 L31 from Kamil with the ablation spherules featured in Fig. 2c, 2d and 2f of Badyukov and Rajtala (2012). Indeed, their Ni contents are different, reflecting different contents in the parent meteorites ($\text{Ni} = 5.87$ vs 20.6 wt% in Sikhote Alin and Gebel Kamil, respectively). To our knowledge, with the exception of a brief mention by Buchwald (1975) reporting on rare occurrences (namely, olivine associated with chromite) from an earlier unqualified resource, silicate inclusions in Sikhote Alin are not documented. Therefore, if confirmed, the occurrence of silicate matrix needs explanation. One possibility is that the silicate matrix is target contamination and therefore that the ablation spherules from Sikhote Alin are impact spherules rather than ablation spherules.

Discrimination of Fe-Ni oxide impact spherules, ablation spherules and I-type cosmic spherules resulting from melting and oxidation of meteoritic iron is thus not straightforward, based on mineralogic and major element geochemical analyses. Target contamination, like geochemical signatures and/or accreted target material, is, however, a strong discriminating factor; evidence for this can be found not just in the sectioned particles but and mainly through careful investigations of their external surfaces.

5. Conclusions

The present mineralogical and geochemical investigation shows that the microscopic Fe-Ni oxide spherules found abundantly in the soil around the 45-m diameter Kamil crater are impact melt spherules formed through the interaction between projectile and target rock melts and air. They add to the inventory of the impact melt ejecta produced by the hypervelocity impact of the Gebel Kamil iron meteorite onto a Cretaceous sandstone target.

The 25 Fe-Ni spherules studied in this work range in size from 100 to 500 μm , have a high degree of sphericity, a variety of dendritic textures and mineral compositions dominated by either Fe-Ni oxides of the Ni-wüstite-trevorite-Ni-magnetite series or homogenous Fe-Ni metal indicating formation through quenching of high temperature (>1600 – 1500 °C; Raghavan 2010; Yang et al. 1996) metallic or metal-oxide liquid droplets under variably oxidizing conditions. Despite large textural and compositional

variations and oxidation conditions, the Fe-Ni spherules share the geochemical signature of the Gebel Kamil iron impactor and target contamination. The geochemical fingerprint of the impactor is provided by the Fe, Co, Ni ratios, well recorded in the compositions of the constituent oxides of the entire spherule population. The average Ni/Co ratio of 25.1 ± 7.6 is consistent with that of Gebel Kamil 27.1 (Table 4). The Ni/(Ni + Fe) molar ratio varies widely from 0.01 to ~ 0.5 (Table 4) as a result of fractionation during the projectile-target melt interaction under oxidizing conditions; nonetheless, their average value of 0.21 ± 0.13 is indistinguishable from that of the bulk impactor of 0.20 (Table 4). Target contamination is documented by the consistent occurrence of elements characteristic of the target only, like Si and Al in the constituent oxides and matrix (Fig. 12; Table 4).

We propose a formation scenario in which Fe-Ni oxide spherules first originated as immiscible blebs of projectile metallic melts within target silicate melts during the projectile-target melt interaction at the transition from the contact and compression stage to the excavation stage, in the crater forming event (Fig. 14). Separation as individual spherules from the host silicate glass with contrasting density occurred by stripping during hypervelocity ejection. We suggest that the model proposed here for the formation of individual Fe-Ni oxide spherules applies to all the small impact events produced by iron or stony-iron impactors and that such spherules should be common impact products, even though, so far, they have only been reported at Barringer Crater (e.g., Kelly et al., 1974), and possibly at Whitecourt (Alberta, Canada) (Kofman et al., 2010).

This work extends the inventory of natural Fe-Ni metal-oxide spherules in the geological record. Similar objects include I-type cosmic spherules (e.g., Genge et al., 2017) and iron meteorite ablation spherules (Badykov and Rajtala, 2012). Target contamination in the form of geochemical signature and/or accreted debris during ballistic ejection are the principal factors discriminating Fe-Ni metal-oxide spherules of impact origin. The higher resistance to weathering of impact Fe-Ni metal-oxide spherules relative to other impact melt microscopic products, often of silicate compositions, make them likely to survive in the stratigraphic record of impact craters produced by iron impactors.

Declaration of Competing Interest

The authors declare that they have no known competing financial interests or personal relationships that could have appeared to influence the work reported in this paper.

Acknowledgements

This work was supported by the Italian Ministero degli Affari Esteri – Progetti di Grande Rilevanza, Protocollo Esecutivo ITALIA-EGITTO (PGR 00107). The 2010 geophysical expedition work was carried out within the framework of the 2009 Italian-Egyptian Year of Science and Technology. Randa Ishak (CISUP, Università di Pisa, Italy), Andrea Risplendente (UNITECH, Università di Milano, Italy), Valentina Batanova (ISTerre, Université Grenoble Alpes, France) and Daniela Mauro (Museo di Storia Naturale, Università di Pisa, Italy) are thanked for technical assistance during FEG-SEM, EPMA and Raman analyses, respectively. ISTerre is part of Labex OSUG@2020 (ANR10 LABX56). Wolf Uwe Reimold, Christopher Hamann and an anonymous reviewer are thanked for reviewing the manuscript and Chris Herd for editorial assistance.

Appendix A. Supplementary material

Supplementary material to this article can be found online at <https://doi.org/10.1016/j.gca.2022.06.035>.

References

- Badykov, D.D., Rajtala, J., 2012. Ablation spherules in the Sikhote Alin meteorite and their origins. *Petrology* 20, 520–528.
- Blau, P.J., Axon, H.J., Goldstein, J.I., 1973. Investigation of the Canyon Diablo metallic spheroids and their relationship to the breakup of the Canyon Diablo meteorite. *J. Geophys. Res.* 78, 363–374.
- Brett, R., 1967. Metallic spherules in impactite and tektite glasses. *Am. Mineral.* 32, 721–733.
- Brownlee, D.E., Bates, B., 1983. Meteor ablation spherules as chondrule analogs. In: King, E.A. (Ed.), *Chondrules and their Origins*. Lunar and Planetary Institute, pp. 10–25.
- Buchwald, V.F., 1975. *Handbook of Iron Meteorites* (3 volumes). University of California Press, Berkeley, USA, p. 1416.
- Bunch, T.E., Cassidy, W.A., 1972. Petrographic and electron microprobe study of the Monturaqui impactite. *Contrib. Mineral. Petrol.* 36, 95–112.
- D'Orazio, M., Folco, L., Zeoli, A., Cordier, C., 2011. Gebel Kamil: The iron meteorite that formed the Kamil Crater (Egypt). *Meteorit. Planet. Sci.* 46, 1179–1196.
- Dredge, I., Parnell, J., Lindgren, P., Bowden, S., 2010. Elevated flux of cosmic spherules (micrometeorites) in Ordovician rocks of the Durness Group, NW Scotland. *Scottish J. Geol.* 46, 7–16.
- Ebert, M., Hecht, L., Deutsch, A., Kenkmann, T., Wirth, R., Berndt, J., 2014. Geochemical processes between steel projectiles and silica-rich targets in hypervelocity impact experiments. *Geochim. Cosmochim. Acta* 133, 257–279.
- Fazio, A., Folco, L., D'Orazio, M., Frezzotti, M.L., Cordier, C., 2014. Shock metamorphism and impact melting in small impact craters on Earth: Evidence from Kamil Crater, Egypt. *Meteorit. Planet. Sci.* 49, 2175–2200.
- Fazio, A., D'Orazio, M., Cordier, C., Folco, L., 2016. Target-projectile interaction during impact melting at Kamil Crater, Egypt. *Geochim. Cosmochim. Acta* 18, 33–50.
- Folco, L., Cordier, C., 2015. Micrometeorites. In: Lee, M.R., Leroux, H. (Eds.), *Planetary Mineralogy*, vol. 15. European Mineralogical Union Notes in Planetary Mineralogy, pp. 253–297.
- Folco, L., D'Orazio, M., Fazio, A., Cordier, C., Zeoli, A., van Ginneken, M., Barkooby, A., 2015. Microscopic impactor debris in the soil around Kamil Crater (Egypt): inventory, distribution, total mass and implications for the impact scenario. *Meteorit. Planet. Sci.* 50, 382–400.
- Folco, L., Di Martino, M., El Barkooby, A., D'Orazio, M., Lethy, A., Urbini, S., Nicolosi, I., Hafez, M., Cordier, C., van Ginneken, M., Zeoli, A., Radwan, A.M., El Khrepy, S., El Gabry, M., Gomaa, M., Barakat, A.A., Serra, R., El Sharkawi, M., 2010. The Kamil Crater in Egypt. *Science* 329, 804.
- Folco, L., Di Martino, M., El Barkooby, A., D'Orazio, M., Lethy, A., Urbini, S., Nicolosi, I., Hafez, M., Cordier, C., van Ginneken, M., Zeoli, A., Radwan, A.M., El Khrepy, S., El Gabry, M., Gomaa, M., Barakat, A.A., Serra, R., El Sharkawi, M., 2011. Kamil Crater (Egypt): ground truth for small-scale meteorite impacts on Earth. *Geology* 39, 179–182.
- Genge, M.J., Engrand, C., Gounelle, M., Taylor, S., 2008. The classification of micrometeorites. *Meteorit. Planet. Sci.* 43, 497–515.
- Genge, M.J., Davies, B., Suttle, M.D., van Ginneken, M., Tomkins, A.G., 2017. The mineralogy and petrology of I-type cosmic spherules: Implications for their sources, origins and identification in sedimentary rocks. *Geochim. Cosmochim. Acta* 218, 167–200.
- Glass, B.P., Huber, H., Koeberl, C., 2004. Geochemistry of Cenozoic microtektites and clinopyroxene bearing spherules. *Geochim. Cosmochim. Acta* 68, 3971–4006.
- Gibbons, R.V., Horz, F., Thompson, T.D., Brownlee, D.E., 1976. Metal blebs in Wabar, Monturaqui and Henbury impactites. *Proceedings, 7th Lunar Science Conference. Geochim. Cosmochim. Acta* 7 (Suppl.), 863–880.
- Hamann, C., Hecht, L., Ebert, M., Wirth, R., 2013. Chemical projectile-target interaction and liquid immiscibility in impact glass from the Wabar craters, Saudi Arabia. *Geochim. Cosmochim. Acta* 121, 291–310.
- Hamann, C., Fazio, A., Ebert, M., Hecht, L., Folco, L., Deutsch, A., Wirth, R., Reimold, W.U., 2018. Silicate liquid immiscibility in impact melts. *Meteorit. Planet. Sci.* 53, 1594–1632.
- Hörz, F., Mittlefehldt, D.W., See, T.H., Galindo, C., 2002. Petrographic studies of the impact melts from Meteor Crater, Arizona, USA. *Meteorit. Planet. Sci.* 37, 501–531.
- Kearsley, A., Graham, G., McDonnell, T., Bland, P., Hough, R., Helps, P., 2004. Early fracturing and impact residue emplacement: can modeling help to predict their location in major craters? *Meteorit. Planet. Sci.* 39, 247–265.
- Kellerud, G., 1962. The Fe – Ni – S system. *Carnegie Inst. Washington Yearbook* 61, 144–150.
- Kelly, W.R., Holdsworth, E., Moore, C.B., 1974. The chemical composition of metallic spheroids and metallic particles within impactite from Barringer Meteorite Crater, Arizona. *Geochim. Cosmochim. Acta* 38, 533–543.
- Kofman, R.S., Herd, C.D.K., Froese, D.G., 2010. The Whitecourt meteorite impact crater, Alberta, Canada. *Meteorit. Planet. Sci.* 45, 1429–1445.
- Love, S.G., Brownlee, D.E., 1991. Heating and thermal transformation of micrometeoroids entering the Earth's atmosphere. *Icarus* 89, 26–43.
- Luoma, R., 1995. A Thermodynamic Analysis of the System Fe-Ni-O. *CALPHAD* 19 (3), 279–295.
- Melosh, H.J., 1989. *Impact cratering: A geologic process*. Oxford Monographs on Geology and Geophysics 11. Oxford University Press, Oxford, p. 245.
- Mittlefehldt, D.W., Hörz, F., See, T.H., Scott, E.R.D., Mertzman, S.A., 2005. Geochemistry of target rocks, impact-melt particles, and metallic spherules from Meteor Crater, Arizona: empirical evidence of the impact process. Large

- Meteorite Impacts III, Geological Society of America Special Paper vol. 384, 367–390.
- Nininger, H.H., 1956. Arizona's Meteorite Crater. American Meteorite Museum, Sedona, p. 232.
- Onoue, T., Nakamura, T., Haranosono, T., Yasuda, C., 2011. Composition and accretion rate of fossil micrometeorites recovered in Middle Triassic deep-sea deposits. *Geology* 39, 567–570.
- Osinski, G.R., Pierazzo, E., 2013. Impact cratering: processes and products. In: Osinski, G.R., Pierazzo, E. (Eds.), *Impact Cratering*. Wiley-Blackwell, Chichester, West Sussex, U.K., pp. 1–20.
- Raghavan, V., 2010. Fe-Ni-O (Iron-Nickel-Oxygen). *J. Ph. Equilibria Diffus.* 31, 369–371.
- Righter, Kevin, Righter, K., Drake, M.J., Yaxley, G., 1997. Prediction of siderophile element metal-silicate partition coefficients to 20GPa and 2800 C: the effects of pressure, temperature, oxygen fugacity, and silicate and metallic melt composition. *Phys. Earth Planet. Inter.* 100, 115–134.
- Rinehart, J.S., 1957. Distribution of meteoritic debris about the Arizona meteorite crater. *Smithsonian Contrib. Astrophysics* 2, 145–160.
- Schmitz, B., 2013. Extraterrestrial spinels and the astronomical perspective on Earth's geological record and evolution of life. *Chem. Erde* 73, 117–145.
- Suttle, M.D., Genge, M.J., 2017. Diagenetically altered fossil micrometeorites suggest cosmic dust is common in the geological record. *Earth Planet. Sci. Lett.* 476, 132–142.
- Tomkins, A.G., Bowlt, L., Genge, M., Wilson, S.A., Brand, H.E.A., Wykes, J.L., 2016. Ancient micrometeorites suggestive of an oxygen-rich Archaean upper atmosphere. *Nature* 533, 235–238.
- Urbini, S., Nicolosi, I., Zeoli, El Khrepy, S., Lethy, A., Hafez, M., El Gabry, M., El Barkooky, A., Barakat, A., Gomaa, M., Radwan, A., El Sharkawi, M., D'Orazio, M., Folco, L., 2012. Geological and geophysical investigation of Kamil Crater, Egypt. *Meteorit. Planet. Sci.* 47, 1842–1868.
- Voldman, G.G., Genge, M.J., Albanesi, G.L., Barnes, C.R., Ortega, G., 2013. Cosmic spherules from the Ordovician of Argentina. *Geol. J.* 48, 222–235.
- Yang, C.-W., Williams, D.B., Goldstein, J.I., 1996. A revision of the Fe-Ni phase diagram at low temperature. *J. Phase Equil.* 17, 522–531.